

The Ocean Mesoscale Regime of the Reduced-Gravity Quasigeostrophic Model

R. M. SAMELSON, D. B. CHELTON, AND M. G. SCHLAX

College of Earth, Ocean, and Atmospheric Sciences, Oregon State University, Corvallis, Oregon

(Manuscript received 6 December 2018, in final form 10 July 2019)

ABSTRACT

A statistical-equilibrium, geostrophic-turbulence regime of the stochastically forced, one-layer, reduced-gravity, quasigeostrophic model is identified in which the numerical solutions are representative of global mean, midlatitude, open-ocean mesoscale variability. Solutions are forced near the internal deformation wavenumber and damped linearly and by high-wavenumber enstrophy dissipation. The results partially rationalize a recent semiempirical stochastic field model of mesoscale variability motivated by a global eddy identification and tracking analysis of two decades of satellite altimeter sea surface height (SSH) observations. Comparisons of model results with observed SSH variance, autocorrelation, eddy, and spectral statistics place constraints on the model parameters. A nominal best fit is obtained for a dimensional SSH stochastic-forcing variance production rate of $1/4 \text{ cm}^2 \text{ day}^{-1}$, an SSH damping rate of $1/62 \text{ week}^{-1}$, and a stochastic forcing autocorrelation time scale near or greater than 1 week. This ocean mesoscale regime is nonlinear and appears to fall near the stochastic limit, at which wave-mean interaction is just strong enough to begin to reduce the local mesoscale variance production, but is still weak relative to the overall nonlinearity. Comparison of linearly inverted wavenumber–frequency spectra shows that a strong effect of nonlinearity, the removal of energy from the resonant linear wave field, is resolved by the gridded altimeter SSH data. These inversions further suggest a possible signature in the merged altimeter SSH dataset of signal propagation characteristics from the objective analysis procedure.

1. Introduction

And we are born and born again

Like the waves of the sea

(P. Simon, “Señorita with a Necklace of Tears”)

The interior ocean mesoscale supports energetic velocity and sea surface height (SSH) variability (Fig. 1) that is typically at least an order of magnitude greater than the long-term mean currents and their geostrophic SSH signatures, and is often described as a form of geostrophic turbulence (The MODE Group 1978; Rhines 1975; see also references in Samelson et al. 2014, 2016). Lateral eddy fluxes driven by this mesoscale variability are poorly understood and a major uncertainty in our understanding of the ocean’s role in Earth’s climate system. Wavenumber–frequency spectra of mesoscale ocean SSH variability from satellite altimeter

measurements typically show an apparent mix of wave and turbulent dynamics: a nondispersive spectral structure (e.g., Zang and Wunsch 1999; Fu and Chelton 2001; Fu 2004; Wunsch 2009; Chelton et al. 2011a) with an effective phase speed that is loosely consistent with phase speeds of theoretical linear, gravest-mode, long-wave, planetary waves (Chelton and Schlax 1996), but an apparent absence of the dispersive decrease in frequency that would be predicted by linear theory (e.g., Killworth et al. 1997; Fu and Chelton 2001; Tailleux and McWilliams 2001) at scales near and smaller than the deformation radius wavelength (Fig. 2a). A number of recent modeling studies have explored the possible origins of this spectral structure (e.g., Early et al. 2011; Berloff and Kamenkovich 2013; Wortham and Wunsch 2014; Morten et al. 2017; LaCasce 2017), and have shown it to be qualitatively consistent both with a geostrophically turbulent eddy field and with isolated, coherent, nonlinear eddy propagation. However, the rapid decline in spectral power with decreasing scale (increasing wavenumber magnitude) and the limited wavelength resolution of presently available SSH fields constructed from satellite altimeter data (see, e.g., appendix A of Chelton et al. 2011b) have hindered

 Denotes content that is immediately available upon publication as open access.

Corresponding author: R. M. Samelson, rsamelson@coas.oregonstate.edu

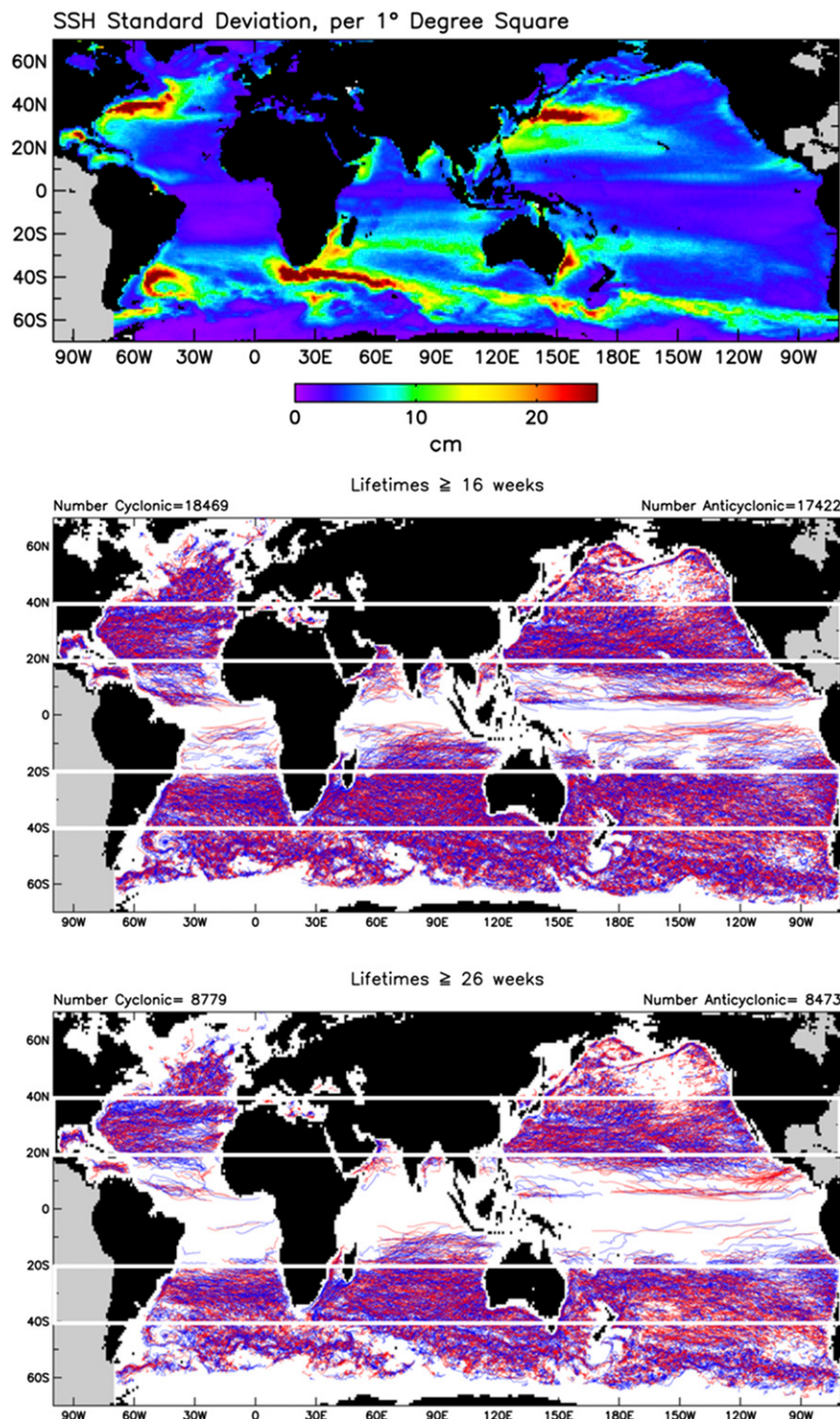


FIG. 1. (top) AVISO SSH standard deviation and (middle),(bottom) eddy tracks for eddies with lifetimes of at least 16 and 26 weeks, respectively, with the latitude ranges 20° – 40° N and 20° – 40° S indicated (white boxes). After [Chelton et al. \(2011b\)](#).

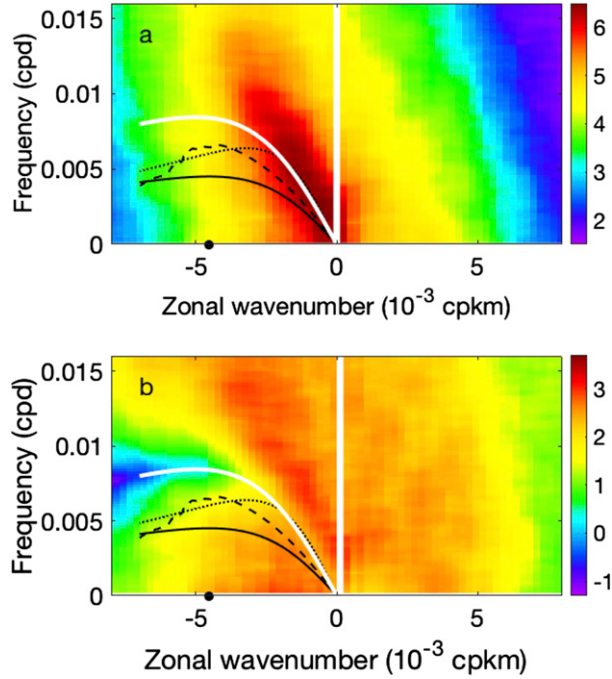


FIG. 2. (a) Power spectrum $|\hat{\eta}_*|^2$ ($\text{cm}^2 \text{cpd}^{-1} \text{cpkm}^{-1}$) and (b) inverted power spectrum $\mathcal{L}_*^{-1} |\hat{\eta}_*|^2$ ($\text{cm}^2 \text{week}^{-2} \text{cpd}^{-1} \text{cpkm}^{-1}$) of SSH variability along 35°S in the south Indian Ocean vs zonal wavenumber and frequency, computed from the approximately 16-yr period October 1992–December 2008 of the AVISO Delayed-Time Reference Series. Also shown are a mean regional deformation radius wavenumber $(2\pi L_R)^{-1}$ for $L_R \approx 35 \text{ km}$ (large black dot) estimated from Fig. 6 of Chelton et al. (1998); three theoretical dispersion relations (black solid, dotted, and dashed, respectively) corresponding to standard Rossby wave theory, the rough bottom topography theory of Tailleux and McWilliams (2001), and the extension by Fu and Chelton (2001) of the vertical shear-modified theory of Killworth et al. (1997) to the case of nonzero zonal wavenumber; and an empirical dispersion relation (white line) of the form $\omega_* = c_{R*} k_* / (\lambda_*^2 k_*^2 + 1)$, with $c_{R*} \approx -0.04 \text{ m s}^{-1}$ and $\lambda_*/(2\pi) \approx 32 \text{ km}$. The raw spectral values have been smoothed in both dimensions, with 3 times more smoothing in the frequency dimension than in the wavenumber dimension. The inverted power spectrum in (b) was computed from the observed spectrum in (a) as described in section 6, using the indicated empirical linear dispersion relation (white line) and dimensional damping $r_* = 1/16 \text{ week}^{-1}$.

determination of the short-wavelength extent of the nondispersive behavior and prevented unambiguous identification of this apparent signature of mesoscale nonlinearity.

From the complementary point of view of eddy phenomenology, a global, quantitative, statistical characterization of midlatitude mesoscale variability has been developed by Chelton et al. (2011b, 2007) from the AVISO (Archivage, Validation, Interpretation des donnees des Satellite Oceanographiques) Delayed-Time Reference Series merged, gridded dataset of two decades of satellite altimeter measurements (Ducet et al. 2000;

Le Traon et al. 2003; Pujol et al. 2016). Because it identifies and tracks coherent features, this eddy-based analysis effectively retains much of the phase information that is discarded when wavenumber-frequency power spectra are computed, and so provides an independent basis of comparison. Recently, Samelson et al. (2016) proposed a linear, stochastic model of mesoscale variability that was able to reproduce nearly all of the basic global mean statistical characteristics of an updated version of the Chelton et al. (2011b) eddy dataset, as well as the nondispersive spectral structure. However, the semiempirical nature of that model made its relation to the physical dynamics unclear, and left a fundamental gap between the theory and the SSH observations.

The goal of the study described here is to take a first step toward reconciling the semiempirical stochastic field model of Samelson et al. (2016) with the simplest standard dynamical model of mesoscale ocean variability, the reduced-gravity quasigeostrophic model (e.g., Pedlosky 1987). While the reduced-gravity vertical structure is highly simplified, it affords a consistent representation of the fundamental potential vorticity dynamics relevant to mesoscale variability and the associated advective nonlinearity, which the semiempirical stochastic model lacks. This work may be seen also as an extension of the related modeling study of Early et al. (2011), in which observed eddy variability was compared with reduced-gravity quasigeostrophic model simulations seeded with random distributions of Gaussian eddies having statistical characteristics drawn from the observed eddy distributions, and of the recent, much more broadly aimed study of the nondispersive spectral structure and statistical equilibrium characteristics of geostrophic turbulence in the reduced-gravity quasi-geostrophic model by Morten et al. (2017), which provided the quantitative framework and starting point for the numerical simulations described here. In addition, this work is related in a more general way to many other previous studies of geostrophic turbulence and quasi-geostrophic models of mesoscale flows.

2. Formulation

In standard dimensionless form, the reduced-gravity quasigeostrophic potential vorticity equation for the velocity streamfunction ψ is

$$\frac{\partial}{\partial t}(\nabla^2 \psi - F_1 \psi) + \beta \frac{\partial \psi}{\partial x} + J(\psi, \nabla^2 \psi) = \mathcal{F} + \mathcal{D}, \quad (1)$$

in which distance and velocity have been scaled respectively by a suitable length L and speed U , time by L/U , streamfunction by UL , and the forcing \mathcal{F} and

damping \mathcal{D} by U^2/L^2 . The dimensionless parameters in (1) are $F_1 = L^2/L_R^2$, $\beta = \beta_* L^2/U$, where L_R is the deformation radius and β_* is the meridional gradient of the Coriolis parameter, and the notation $J(\cdot, \cdot)$ denotes the Jacobian derivative. In the reduced-gravity interpretation, $L_R = (g'H)^{1/2}/f$, where $g' = g \Delta\rho/\rho_0$ is the reduced gravity for a single active layer of thickness H overlying a deep, motionless layer with fixed fractional density difference $\Delta\rho/\rho_0$, $g = 9.81 \text{ m s}^{-2}$ is the acceleration of gravity, and f is the Coriolis parameter.

A stochastic form of the forcing \mathcal{F} has been used in numerous idealized studies of two-dimensional or geostrophic turbulence, following its introduction by Lilly (1969). In the present setting, a physical interpretation of the associated stochastic process is needed. Samelson et al. (2014, 2016) have previously found that the amplitude of the stochastic forcing required to reproduce observed SSH amplitudes in their original eddy life cycle model and subsequent linear field model was much too large to allow interpretation as wind forcing, and that the forcing must instead represent internal dynamical processes. This result holds again for the quasigeostrophic model, in which it must primarily represent baroclinic interactions with an unspecified larger-scale mean flow or higher-order vertical modes, with small, supplemental contributions from wind and other external forcing processes.

For the case of stochastic forcing, (1) may be written as a stochastic differential equation for the potential vorticity q on the characteristics defined by the velocity field,

$$dq = \sigma_{\mathcal{F}} dW_t + \mathcal{D} dt \quad \text{on} \quad \left(\frac{dx}{dt}, \frac{dy}{dt} \right) = \left(-\frac{\partial\psi}{\partial y}, \frac{\partial\psi}{\partial x} \right), \quad (2)$$

where

$$q = \nabla^2\psi - F_1\psi + \beta y, \quad (3)$$

$\sigma_{\mathcal{F}}$ is a constant and W_t is the Wiener process (i.e., standard continuous Brownian motion). For numerical solution, the Wiener process is replaced here by

$$\sigma_{\mathcal{F}} dW_t = \sigma_{\mathcal{F}} \frac{\mathcal{F}_0(x, y, t/\tau)}{\tau^{1/2}} dt = \mathcal{F} dt, \quad (4)$$

where $\mathcal{F}_0(x, y, t/\tau)$ is a smooth stochastic function with unit time-mean spatial standard deviation and autocorrelation time scale τ , and the second equality defines \mathcal{F} in (1). The factor $1/\tau^{1/2}$ in (4) ensures that the expectation value of the time integral of the variance of \mathcal{F} is equal to $\sigma_{\mathcal{F}}^2 t$ for $t \gg \tau$, consistent with (2). The numerical implementation of \mathcal{F}_0 follows Morten et al. (2017), as does the specification of \mathcal{D} as the sum of a

linear damping on ψ and a triharmonic term to smooth the small scales,

$$\mathcal{D} = r_\psi \psi - r_6 \nabla^6 \psi, \quad (5)$$

with constant damping coefficients r_ψ and r_6 .

The dimensional scales L and U may be chosen to reduce the number of dimensionless parameters in (1)–(5). Setting

$$L = L_R, \quad U = \sigma_{\mathcal{F}*}^{2/3} L_R, \quad (6)$$

where $\sigma_{\mathcal{F}*}$ is the dimensional equivalent of $\sigma_{\mathcal{F}}$, effectively sets $F_1 = 1$ and $\sigma_{\mathcal{F}} = 1$, yielding (1) in the reduced form considered here:

$$\begin{aligned} & \frac{\partial}{\partial t} (\nabla^2 \psi - \psi) + \beta \frac{\partial \psi}{\partial x} + J(\psi, \nabla^2 \psi) \\ &= \frac{\mathcal{F}_0(x, y, t/\tau)}{\tau^{1/2}} + r_\psi \psi - r_6 \nabla^6 \psi. \end{aligned} \quad (7)$$

In (7), there are three parameters of primary physical interest: β , r_ψ , and τ . The spatial structure of the forcing function \mathcal{F}_0 , which must also be specified, is taken to have the same form as in Morten et al. (2017), with forcing restricted to wavenumbers in an annulus of width $\delta K = 1/3$ around the deformation radius wavenumber $K = 1$, while the constant r_6 is chosen as a small value sufficient to maintain smoothness at small scales. If τ is sufficiently small relative to the intrinsic time scales of the flow, the solution should be insensitive to its value. However, τ is a fundamental descriptor of the physical processes represented in the model by the stochastic forcing, and as such is retained here as an independent parameter, rather than held constant as in Morten et al. (2017).

Specification of a reference latitude ϕ determines the corresponding values of the dimensional Coriolis parameter f and its meridional gradient β_* . If a dimensional value of L_R is also specified, then, for a given solution of (7), the value of the velocity scale U can be obtained from the given value of the dimensionless parameter β :

$$U = \frac{\beta_* L_R^2}{\beta}. \quad (8)$$

This in turn allows determination of the dimensional SSH η_* from the dimensionless streamfunction ψ ,

$$\eta_* = fg^{-1}\psi_* = fg^{-1}UL_R\psi = \frac{\beta_* f}{g\beta} L_R^3 \psi, \quad (9)$$

where ψ_* is the dimensional streamfunction, as well as the dimensional linear damping and stochastic forcing rates $r_{\psi*}$ and $\sigma_{\mathcal{F}*}$:

$$r_{\psi*} = \frac{U}{L_R} r_\psi = \frac{\beta_* L_R}{\beta} r_\psi, \quad (10)$$

$$\sigma_{\mathcal{F}*} = \left(\frac{U}{L_R} \right)^{3/2} = \left(\frac{\beta_* L_R}{\beta} \right)^{3/2}. \quad (11)$$

Equation (7) may be written in terms of the dimensional SSH,

$$\left(\frac{\partial}{\partial t_*} - \beta_* \frac{\partial}{\partial x_*} \right) \eta_* = \mathcal{F}_{*SSH} \mathcal{F}_0 + \text{other terms}, \quad (12)$$

where the dimensional SSH forcing scale is

$$\mathcal{F}_{*SSH} = \frac{\sigma_W}{\tau_*^{1/2}}, \quad (13)$$

for $\tau_* = T\tau$ and

$$\sigma_W = \frac{fL_R^2}{g} \sigma_{\mathcal{F}*} = \frac{fL_R^{7/2}}{g} \left(\frac{\beta_*}{\beta} \right)^{3/2}. \quad (14)$$

Values of σ_W may be compared directly with those characterizing the forcing rate for the semiempirical models of Samelson et al. (2014, 2016), which were based on long-wave versions of (12).

Numerical solutions of (7) were computed on a 256×128 zonal–meridional grid with periodic boundary conditions, using a nonaliasing pseudospectral code originally derived from the two-layer channel model described by Samelson and Pedlosky (1990) and Oh et al. (1993). Guided by the considerations described in section 3, two primary sets of simulations were conducted, with integrations generally to dimensionless $t = 1160$ for the first set and $t = 625$ for the second set, corresponding to dimensional times of roughly 30 and 37.5 years, respectively. A dimensionless integration time of up to $t \approx 50$, equivalent to a dimensional time of 1–3 years, was typically required for the numerical solutions to reach statistical equilibrium (Fig. 3). The autocorrelation and spectral analyses were conducted on output-field time series of length 2048, and the eddy analysis on output-field time series of length 1025, for dimensionless output time increments of 0.46 for the first set and 0.25 for the second set, corresponding to dimensional output time increments of 4.4 and 5.5 days, respectively. For the eddy identification and tracking analysis, the model SSH field was tiled periodically and interpolated onto a 512×128 grid with uniform zonal and meridional spacing $\Delta x_* = \Delta y_* = 15.12$ km, identical to the domain used by Samelson et al. (2016) for the eddy analysis of the linear stochastic model SSH fields.

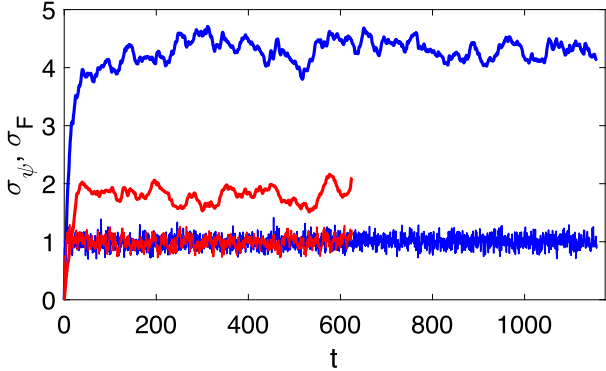


FIG. 3. Spatial standard deviation of dimensionless sea surface height $\sigma_\eta(t)$ (thick lines) and forcing amplitude $\sigma_{\mathcal{F}}(t)$ (thin, with $\sigma_F \approx 1$) vs dimensionless time t from simulations with $\beta = 0.62$, $\tau = 0.92$, $r_\psi = 0.022$ (blue) and $\beta = 2.40$, $\tau = 5.00$, $r_\psi = 0.024$ (red).

Coherent eddies in the model fields were identified and tracked, after conversion of ψ to dimensional SSH η_* , using the same updated version of the Chelton et al. (2011b) SSH-based procedure described by Samelson et al. (2016). At each time point along an identified eddy track, the procedure produces an eddy amplitude, length scale, and rotational speed, as well as an index identifying the eddy as cyclonic or anticyclonic. The amplitude is defined as the difference between the maximum SSH within the eddy and the mean SSH around the outermost closed contour of SSH, and the eddy track point location is defined as the centroid of SSH computed over all grid points within that contour. The length scale is the radius of a circle with area equivalent to that contained by the closed SSH contour with maximum mean geostrophic speed, and the rotational speed scale is that mean geostrophic speed. Consistent with Chelton et al. (2011b), the amplitude, length scale, and rotational speed statistics discussed below were computed for eddies with lifetimes of at least 16 weeks.

3. The ocean mesoscale parameter regime

a. Analytical estimates

The original starting point for these simulations was provided by the “Run 3” simulation of Morten et al. (2017), which was identified by those authors as likely to be the most representative of the ocean mesoscale among their set of simulations. For the scaling of (1) used by Morten et al. (2017), the Run 3 simulation had parameter values $\beta_{M3} = 10$, $k_d = F_1^{1/2} = 6$, $\tau_{M3} = 0.1$, $r_{M3} = 1.4$. The equivalent parameter values for (7) are $\beta = \beta_{M3}/(k_d \tau_{M3}^{1/3}) = 3.59$, $\tau = \tau_{M3}^{4/3} = 0.0464$, $r_\psi = r_{M3}/(k_d^2 \tau_{M3}^{1/3}) = 0.084$ (see appendix). Preliminary results from initial simulations conducted with these

Run 3 parameters provided the basis and rationale for the set of simulations reported here.

Subsequently, an analytical approach was developed to refine the estimate of the appropriate parameter regime for these ocean mesoscale simulations. In the stochastic limit $\tau \ll 1$, an integration of (2) over the autocorrelation time τ gives

$$q(t + \tau) - q(t) \approx \delta_{\mathcal{F}} + r_{\psi} \psi(t) \tau, \quad (15)$$

where $\delta_{\mathcal{F}} = \mathcal{F}_0 \tau^{1/2}$ is the stochastic increment with ensemble-averaged (or t -averaged) variance $\langle \delta_{\mathcal{F}}^2 \rangle = \tau$ for $\sigma_{\mathcal{F}} = 1$, and the enstrophy dissipation term has been neglected for simplicity, so that $\mathcal{D} = r_{\psi} \psi$. If an appropriately weighted mean wavenumber \bar{K} may be chosen so that $q(t + \tau) - q(t) \approx -(\bar{K}^2 + 1) [\psi(t + \tau) - \psi(t)]$, the resulting ensemble-averaged variance equation may be further approximated as

$$(\bar{K}^2 + 1)^2 \langle \psi(t + \tau)^2 \rangle \approx (\bar{K}^2 + 1 - r_{\psi} \tau)^2 \langle \psi(t)^2 \rangle + \tau. \quad (16)$$

An equivalent result can be obtained from an integration of the energy equation for (7), under the assumption that ψ is effectively constant on the time scale τ except for a directly forced component proportional to $\mathcal{F}t$. At statistical equilibrium, the ensemble-averaged variance of ψ is stationary, and it then follows from (16) that for $r_{\psi} \tau \ll 1$, the standard deviation σ_{ψ} of ψ can be estimated as

$$\sigma_{\psi} \approx \frac{1}{[2(\bar{K}^2 + 1) r_{\psi}]^{1/2}}. \quad (17)$$

Thus, in the stochastic limit, and under the assumption that the potential vorticity variance is concentrated near the deformation wavenumber $K = 1$, the dimensionless streamfunction standard deviation σ_{ψ} is approximately equal to one-half of the inverse square root of the dimensionless damping rate.

A second relation between σ_{ψ} and r_{ψ} , which depends upon dimensional parameters, may be derived and then combined with (17) to obtain an a priori estimate of the dimensionless parameter values appropriate for the ocean mesoscale regime. The dimensionless quantity σ_{ψ}/β serves as a measure of nonlinearity: with the solution variance again assumed to be concentrated near the deformation wavenumber $K = 1$, the ratio of nonlinear to linear terms in (7) may be estimated as

$$\frac{|J(\psi, \nabla^2 \psi)|}{|\beta \frac{\partial \psi}{\partial x}|} \approx \frac{\sigma_{\psi}}{\beta}. \quad (18)$$

By (9), this ratio is proportional to the standard deviation σ_{η^*} of dimensional SSH:

$$\frac{\sigma_{\psi}}{\beta} = \frac{g}{\beta_* f L_R^3} \sigma_{\eta^*}. \quad (19)$$

In turn, by (10),

$$\frac{r_{\psi}}{\beta} = \frac{r_{\psi^*}}{\beta_* L_R}, \quad (20)$$

and therefore

$$\frac{\sigma_{\psi}}{r_{\psi}} = \frac{g}{f L_R^2} \frac{\sigma_{\eta^*}}{r_{\psi^*}}. \quad (21)$$

With $L_R = c_1/f$ (Fig. 4a), where $c_1 \approx 3 \text{ m s}^{-1}$ is a fixed, nominal value of the gravest-mode internal gravity wave speed (e.g., Chelton et al. 1998), the first factors on the right-hand sides of (19) and (21) are known, while σ_{η^*} and r_{ψ^*} must be estimated from observations.

The majority of the eddies in the updated Chelton et al. (2011b) dataset that are not associated with western boundary currents or the Antarctic Circumpolar Current are found between latitudes of 20° and 40°N or between 20° and 40°S (Fig. 1). In these subtropical interior regimes, the standard deviation σ_{η^*} of SSH from the altimeter dataset used by Chelton et al. (2011b) ranges roughly from 0.02 to 0.07 m, with zonal averages that include the western boundary currents and their extensions lying toward the upper end of that range (Figs. 1, 4b). Then, for example, taking $\sigma_{\eta^*} \approx 0.07 \text{ m}$ at $\phi = 35^\circ$ gives $\sigma_{\psi}/\beta \approx 7$ and indicates strong nonlinearity, while taking $\sigma_{\eta^*} \approx 0.02 \text{ m}$ at $\phi = 24^\circ$ gives $\sigma_{\psi}/\beta \approx 0.9$ and indicates moderate nonlinearity (Fig. 4b).

From their model fit to observations, Samelson et al. (2016) estimate a damping rate for η_* or ψ_* as $R \approx 1/25 \text{ week}^{-1}$. This rate could be used directly for r_{ψ^*} in (20) and (21), but an improved estimate is obtained for $r_{\psi^*} \approx 1/50 \text{ week}^{-1}$; effectively, this assumes that the nonlinearity in the present model contributes equally with the damping to the autocorrelation decay, whereas in the linear model of Samelson et al. (2016), all of the autocorrelation decay along long-wave characteristics must derive from the damping. With this nominal value for r_{ψ^*} and with $L_R = c_1/f$ as previously, the ratio r_{ψ}/β depends only on ϕ , taking values of roughly 0.045 at $\phi = 35^\circ$ and 0.028 at $\phi = 24^\circ$ (Fig. 4c).

Combining these two estimates of σ_{ψ}/β and r_{ψ}/β , or substituting the representative values for σ_{η^*} and r_{ψ^*} into (21), gives the linear relations $\sigma_{\psi} \approx (7/0.045) r_{\psi} \approx 155 r_{\psi}$ at $\phi = 35^\circ$ and $\sigma_{\psi} \approx (0.9/0.028) r_{\psi} \approx 32 r_{\psi}$ at $\phi = 24^\circ$. Each of these two equations may then be combined with (17) to obtain two estimates of the dimensionless parameters

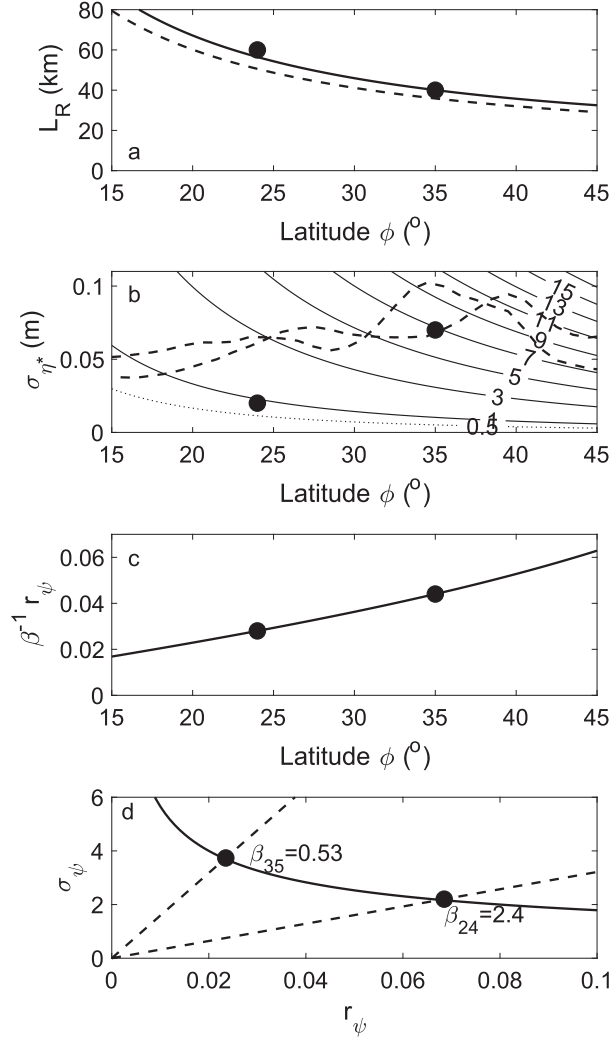


FIG. 4. Ocean mesoscale regime parameters. The points corresponding to the target values for the dimensional comparisons at latitudes $\phi = 35^{\circ}$ and $\phi = 24^{\circ}$ are indicated (black filled circles). (a) Deformation radius $L_R = c_1/f$ vs latitude ϕ for $c_1 = 3.35 \text{ m s}^{-1}$ (solid line) and $c_1 = 3 \text{ m s}^{-1}$ (dashed). (b) Contours (labeled, solid and dotted lines) of σ/β from (17) for $L_R = c_1/f$ with $c_1 = 3.35 \text{ m s}^{-1}$ vs latitude ϕ and specified SSH standard deviation σ_{η}^* . The zonally averaged AVISO SSH standard deviations in the northern and southern hemispheres are also shown (dashed lines). (c) Scaled friction parameter r_{ψ}/β from (20) for $r_{\psi*} \approx 1/50 \text{ week}^{-1}$ and $L_R = c_1/f$ with $c_1 = 3.35 \text{ m s}^{-1}$ vs latitude ϕ . (d) Graphical illustration of the joint solution of (17) and (21) for the dimensionless parameters $(\sigma_{\psi}, r_{\psi}, \beta)$ at latitudes $\phi = 35^{\circ}$ and $\phi = 24^{\circ}$.

r_{ψ} and β at which the solutions with the desired values of σ_{η}^* and σ_{ψ}/β may be found (Fig. 4d). For $\sigma_{\eta}^* \approx 0.07 \text{ m}$ at latitude $\phi = 35^{\circ}$, the estimated values are $(\beta, r_{\psi}) \approx (0.53, 0.02)$, while for $\sigma_{\eta}^* \approx 0.02 \text{ m}$ at latitude $\phi = 24^{\circ}$, the estimated values are $(\beta, r_{\psi}) \approx (2.40, 0.07)$. The corresponding estimated values of σ_{ψ} are roughly 3.7 at $\phi = 35^{\circ}$ and 2 at $\phi = 24^{\circ}$. For these estimates, the value $K = 0.75$ has been used in (17).

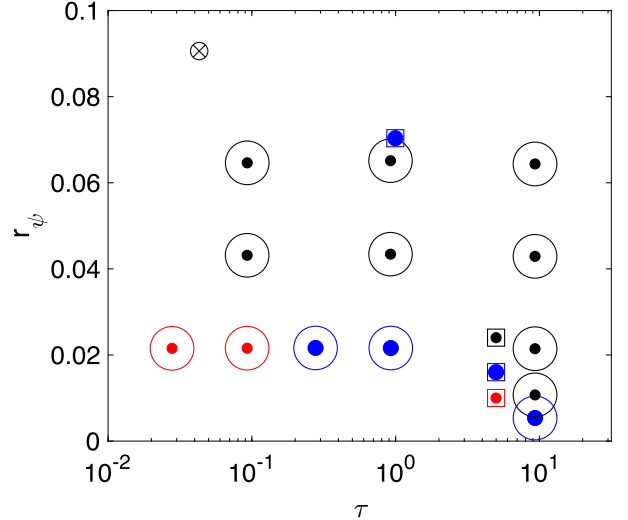


FIG. 5. Summary of values of (τ, r_{ψ}) for simulations with $\beta = 0.62$ (filled circle with enclosing open circle), $\beta = 2.4$ (filled circle with enclosing square), and for the Run 3 simulation (\times with enclosing open circle) of Morten et al. (2017). Simulations with σ_{ψ}/β within 5% of the respective target values $\sigma_{\psi}/\beta = \{7, 0.9\}$ for $\beta = \{0.62, 2.4\}$ (blue, large filled circle), more than 5% greater than the target values (red), and less than 95% of the target values (black) are indicated.

Along with the damping time scale $R \approx 1/25 \text{ week}^{-1}$, Samelson et al. (2016) estimate a dimensional value of $2.5 \times 10^{-5} \text{ m s}^{-1/2}$ for σ_W . For $L_R = 40$ at $\phi = 35^{\circ}$ (Fig. 4a), this corresponds by (11) to $\sigma_{\mathcal{F}*} = (g/fL_R^2)\sigma_W \approx 1.8 \times 10^{-9} \text{ s}^{-3/2}$, and thus to $U \approx 0.06 \text{ m s}^{-1}$ by (8) and to dimensionless parameters $\beta \approx 0.5$, $r_{\psi} = RL_R/U \approx 0.04$, $\tau = \Delta t U/L_R \approx 0.9$, where the autocorrelation time scale is derived from the Samelson et al. (2016) discrete time step $\Delta t = 1$ week. For $L_R = 60 \text{ km}$ at $\phi = 24^{\circ}$, the same values of σ_W , R , and Δt give $\sigma_{\mathcal{F}*} \approx 1.15 \times 10^{-9} \text{ s}^{-3/2}$, $U = 0.066 \text{ m s}^{-1}$, and $\beta \approx 1.1$, $r_{\psi} \approx 0.06$, $\tau \approx 0.67$. This provides an alternative point of reference for the relevant model parameter values.

Guided by these considerations, two primary sets of simulations were conducted, in each of which β was held fixed while r_{ψ} and τ were varied (Fig. 5). The first set, with $\beta = 0.62$, was directed toward reproducing a more strongly nonlinear regime, with dimensional SSH standard deviation $\sigma_{\eta}^* = 0.07 \text{ m}$ for $L_R = 40 \text{ km}$ at a nominal latitude $\phi = 35^{\circ}$. For this set, the dimensional velocity and time scales are $U \approx 0.05 \text{ m s}^{-1}$ and $T = L_R/U \approx 8.2 \times 10^5 \text{ s} \approx 9.5 \text{ days}$, and the dimensional forcing amplitude is $\sigma_{\mathcal{F}*} = T^{-3/2} \approx 1.3 \times 10^{-9} \text{ s}^{-3/2}$, equivalent to $\sigma_W \approx 1.8 \times 10^{-5} \text{ m s}^{-1/2}$. The second set, with $\beta \approx 2.4$, was directed toward reproducing a more moderately nonlinear regime, with dimensional SSH standard deviation $\sigma_{\eta}^* = 0.02 \text{ m}$ for $L_R = 60 \text{ km}$ at a nominal latitude $\phi = 24^{\circ}$. For this set, the dimensional

velocity and time scales are $U \approx 0.03 \text{ m s}^{-1}$ and $T = L_R/U \approx 1.9 \times 10^6 \text{ s} \approx 22 \text{ days}$, and the dimensional forcing amplitude is $\sigma_{\mathcal{T}^*} \approx 0.4 \times 10^{-9} \text{ s}^{-3/2}$, equivalent to $\sigma_W \approx 0.8 \times 10^{-5} \text{ m s}^{-1/2}$. A number of additional simulations were conducted, of which only the equivalent to the Morten et al. (2017) Run 3 is described here. With the stochastic-limit estimate (17), the Morten et al. (2017) Run 3 simulation can be anticipated to have $\sigma_\psi \approx 1.7$ and $\sigma_\psi/\beta \approx 0.5$, and thus to be less nonlinear than the moderately nonlinear estimate $\sigma_\psi/\beta \approx 0.9$ obtained for $\sigma_{\eta^*} \approx 0.02 \text{ m}$ at latitude $\phi = 24^\circ$.

b. Eddy phenomenology

Tracked eddies in these simulations show several distinctive characteristics that may be taken to define their overall phenomenology, including dominance of advective rearrangement over direct forcing of the potential vorticity field, sustained westward propagation modulated by modest departures from the linear long-wave trajectory, periods of relative stability punctuated by abrupt change, and continuous interaction of eddy structures with their surroundings. The resulting phenomenological picture differs distinctly from that of a single isolated eddy dominated by linear planetary-wave propagation and nonlinear self-interaction, and as such is much closer, for example, to the random eddy-seeded simulations of Early et al. (2011) than to the isolated monopole simulations in that same study or others (e.g., Larichev and Reznik 1976; McWilliams and Flierl 1979). In its complexity, it resembles qualitatively many previous simulations of two dimensional and geostrophic turbulence (e.g., Lilly 1969; Rhines 1979; McWilliams and Chow 1981; Smith and Vallis 2001, 2002; Arbic and Flierl 2004; Morss et al. 2009; Venaille et al. 2011; Morten et al. 2017; and numerous references therein). Likewise, it is distinct in these ways from the classical baroclinic-growth and barotropic-decay life cycles found in studies of midlatitude synoptic disturbances in the atmosphere (e.g., Simmons and Hoskins 1978).

A useful illustrative example of the complex life cycle of a simulated eddy identified by the tracking procedure is furnished by eddy 4386 from a simulation conducted for $\beta = 0.62$, $r_\psi = 0.022$, and $\tau = 0.92$, with dimensional SSH computed for $L_R = 40 \text{ km}$ at a nominal latitude $\phi = 35^\circ\text{N}$ (Fig. 6). This eddy is anticyclonic (SSH signature $\eta_* > 0$) and has a lifetime of approximately 73 weeks, corresponding to 116 eddy-tracking time steps. The SSH amplitude undergoes three main growth and decay phases over this lifetime, the first during the first 10 weeks and reaching a maximum of 5 cm, and the second and third during weeks 15–35 and 40–65 and reaching a maximum of 13 cm, while fluctuating continuously on shorter time scales. The rotational speed

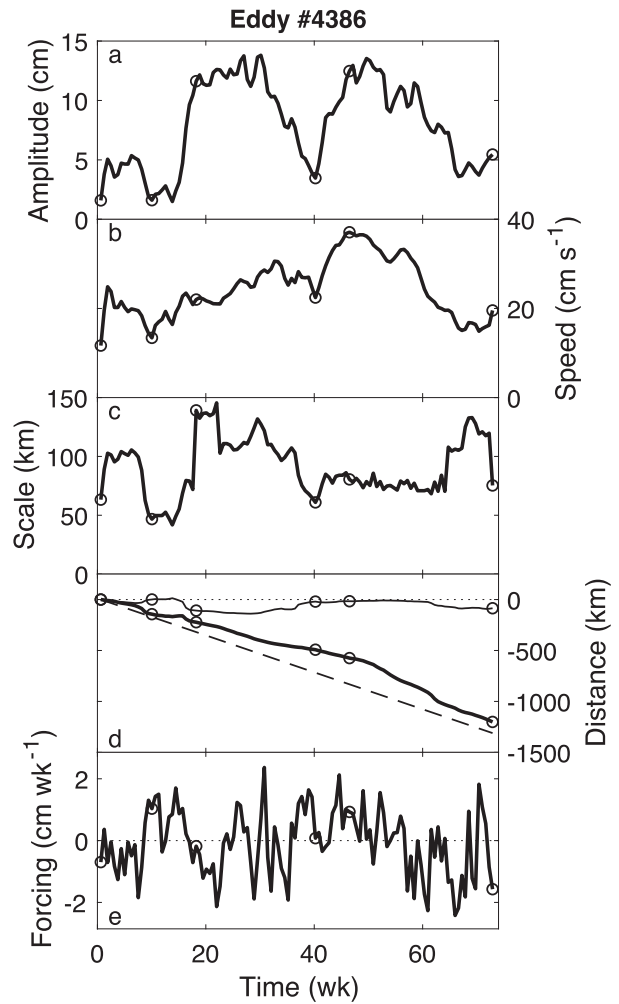


FIG. 6. Time (weeks) history of (a) amplitude, (b) speed, (c) length scale, (d) relative zonal (thick solid line), meridional (thin solid), and theoretical linear long-wave (dashed) displacements, and (e) equivalent-SSH stochastic forcing $\mathcal{T}_{\text{SSH}}^*$ at eddy central point, for tracked eddy 4386 from the solution with $\beta = 0.62$, $r_\psi = 0.022$, $\tau = 0.92$. The times corresponding to the panels in Fig. 7 are indicated (open circles).

scale has less variability than amplitude, remaining between 20 and 35 cm s^{-1} over most of the eddy lifetime. The length scale changes infrequently but more abruptly, with some correlation to the amplitude history but some notable deviations, and remains between 70 and 100 km over most of the eddy lifetime, with extreme values near 50 and 150 km. The eddy propagates zonally at a speed that, in the mean over eddy lifetime, is slightly slower than the linear long-wave speed, but exceeds that speed continuously for three months beginning near week 50. The SSH forcing $\mathcal{T}_{\text{SSH}}^*$ at the centroid point has typical values of $\pm 1 \text{ cm week}^{-1}$ and fluctuates stochastically on the time scale $\tau_* = T\tau \approx 8.7 \text{ days} \approx 1.2 \text{ weeks}$, with no obvious relation to the eddy amplitude history.

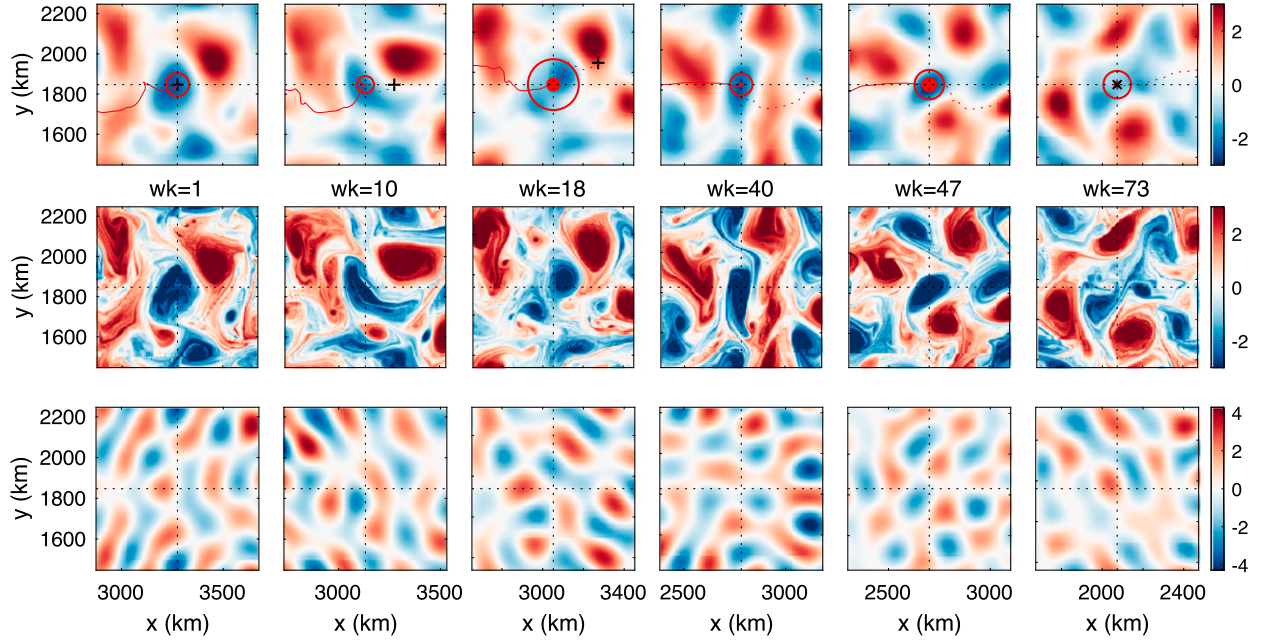


FIG. 7. Scaled dimensionless quasigeostrophic (top) thickness $-F_1\psi/(2\pi\beta)$ and (middle) total disturbance $q'/(2\pi\beta)$ potential vorticities, with (bottom) dimensional stochastic forcing (cm week^{-1}), at times $t_* = \{1, 10, 18, 40, 47, 73\}$ weeks, corresponding to time steps $\{1, 16, 29, 64, 74, 116\}$ over the 116-step life cycle of eddy 4386 from the solution with $\beta = 0.62$, $r_\psi = 0.022$, $\tau = 0.92$. The sign of the forcing is as in the potential vorticity equation (1), rather than for equivalent-SSH forcing as in Fig. 6. The y axes for the five sets of panels after time step 1 are offset relative to the step 1 axes by $\{0.6, -108.3, -20.1, -16.5, -85.3\}$ km, respectively, matching the meridional displacements of the eddy centroid. The eddy relative amplitude (red dot, radius proportional to amplitude) and length scale (red open circle, radius equal to length scale) are indicated in the thickness panels, along with the past (red dotted line, initial point +) and future (red solid, final point ×) trajectory of the eddy.

The structural evolution of eddy 4386 shows several distinct stages that are related to the amplitude history. These stages can be described in terms of the dimensionless thickness [$q_h = -F_1\psi = -g(fUL_R)^{-1}\eta_* < 0$ for this anticyclonic eddy] and total disturbance (PV) fields at a sequence of times along the track, chosen here as steps $\{1, 16, 29, 64, 74, 116\}$ for the 4.4-day tracking time step (Fig. 7). Initially, at step 1, the thickness PV (or SSH) field appears to show a well-formed, roughly symmetric eddy structure, but the total disturbance PV field has an asymmetric structure, which has arisen through a vortex roll-up process that has occurred as the eddy separates from an anticyclonic anomaly located roughly 300 km to its southeast. After an initial period of amplitude growth, by step 16 (week 10) the eddy is distorted and elongated in a southeast–northwest orientation as it evolves under the influence of the surrounding PV anomalies, and the amplitude attributed to it as an isolated coherent feature by the eddy identification procedure decreases to near 1 cm, just above the tracking cutoff minimum. Near step 29 (week 18), the eddy identification procedure correctly anticipates the merger and incorporation into eddy 3486 of a

smaller anticyclonic structure to its southwest, and both the eddy amplitude and length scale increase abruptly. This structure remains relatively stable but is slowly distorted after week 30 toward an elongated north–south structure, with tracked amplitude decaying until it reaches a minimum near 4 cm at step 64 (week 40). Immediately after this minimum is reached, eddy 4386 pairs with an energetic cyclonic disturbance to its southeast (step 74, week 47), and this vortex pair subsequently rotates 1/8-turn clockwise and propagates nearly directly westward for several months at speeds slightly exceeding the linear long-wave speed. Eventually, it overtakes a group of PV anomalies to its west, and ultimately is torn apart through that interaction, with the eddy track ending at step 116 (week 73) as the tracking procedure is unable to identify a suitable coherent feature that satisfies the criteria for continuation of the track.

4. Amplitude and autocorrelation

A basic statistical characterization of each simulation that may be compared directly with observations and with the linear field model results of Samelson et al.

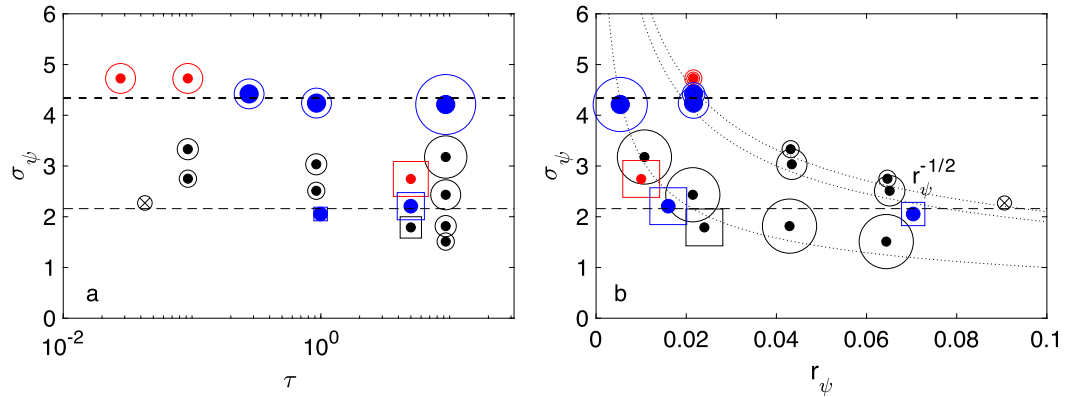


FIG. 8. Time-mean dimensionless streamfunction standard deviation σ_ψ (markers as in Fig. 5) for simulations with $\beta = \{0.62, 2.4\}$ vs (a) τ , with open circle and open square size proportional to $r_\psi^{-1/2}$, and (b) r_ψ , with open circle and open square size proportional to $r^{1/4}$. The target values $\sigma_\psi = \{7, 0.9\}$ $\beta \approx \{4.3, 2.2\}$ for the simulations with $\beta = \{0.62, 2.4\}$, respectively, are indicated (thick and thin dashed lines, respectively). The relation $\psi \propto r_\psi^{1/2}$ is also shown in (b) (dotted lines) for several values of the proportionality constant.

(2016) is provided by the domain-mean amplitude response and autocorrelation scale. For $\beta = 0.62$, the three simulations with $(r_\psi, \tau) = \{(0.022, 0.28), (0.022, 0.92), (0.0054, 9.3)\}$ are within 5% of the amplitude target $\sigma_\psi = 7\beta \approx 4.3$, while for $\beta = 2.4$, the two simulations with $(r_\psi, \tau) = \{(0.07, 1), (0.016, 5)\}$ are within 5% of the amplitude target $\sigma_\psi = 0.9\beta \approx 2.2$ (Fig. 8a).

For $\beta = 0.62$ and $r_\psi = 0.022$, σ_ψ has equal values for the two simulations with the smallest stochastic time scales, $\tau = \{0.028, 0.093\}$, decreases slightly for $\tau = \{0.28, 0.93\}$, and is reduced by half for $\tau = 9.3$, suggesting that the stochastic limit is approached for $\tau \leq 1$ but violated for $\tau \geq 1$, as the stochastic time scale becomes comparable to the intrinsic dynamical time scale and correlations can develop between the forcing and the dynamically evolving field. Because the associated transition occurs for $\tau \approx 1$, this correspondence also indicates that the dimensional time scale $T = L_R/U$ used in the scaling is an accurate estimate of the intrinsic dynamical time scale. Nonetheless, the dependence $\sigma_\psi \propto r_\psi^{-1/2}$ predicted by (17) for solutions with fixed τ and β is approximately reproduced even when $\tau \geq 1$ (Fig. 8b). For $\beta = 0.62$ and $r_\psi = 0.022$, the estimate (17) approximately matches the result from the numerical simulations with $\tau < 1$ if the choice $\bar{K} \approx 0.75$ is made, consistent with a concentration of the solution variance at wavenumbers slightly smaller than the radian deformation wavenumber $k_{d*} = L_R^{-1}$.

For the linear stochastic models of Samelson et al. (2014, 2016), the damping coefficient r determined the temporal autocorrelation parameter α directly, according to $\alpha = 1 - r < 1$, where for the stochastic field model (Samelson et al. 2016), the autocorrelation was computed along long-wave characteristics. Samelson et al. (2014) computed values of α from the observed SSH

along long-wave characteristics, and showed that the values so computed at midlatitudes were approximately 0.95, for time units of weeks, and that these values were much larger than those computed at fixed spatial points. The corresponding values of α computed for the models of Samelson et al. (2014) and Samelson et al. (2016) were 0.96 and 0.94, respectively, in close agreement with the observed values.

For the nonlinear quasigeostrophic model (7), the nonlinearity can alter the autocorrelation, and the parameter α cannot be computed directly from r_ψ . Instead, α must be estimated from the empirical autocorrelation function $A_a(t)$ computed from the model fields, and is taken here as the maximum value of the effective α obtained along characteristics of the form $dx/dt = ac_R$, where $c_R = -\beta$ (with $F_1 = 1$) is the model linear long-wave speed and a is a parameter with $0.5 \leq a \leq 1.0$. The empirical autocorrelation function was assumed to have the form $A_a(t) = \alpha^t$, and the model value α_{eff} was computed as the mean of $A_a(t)^{1/t}$ for $10 \text{ weeks} \leq t \leq 20 \text{ weeks}$, with the optimization using a increments of 0.05 (Fig. 9).

The resulting equivalent damping values $r_\alpha = 1 - \alpha_{\text{eff}}$ are roughly 0.02 week⁻¹ greater than the dimensional model damping $r_{\psi*} = UL_R^{-1} r_\psi$ (Fig. 10). This additional decorrelation found for solutions of (7) relative to the linear stochastic model solutions is evidently the result of the nonlinear, advective, scrambling of the model fields, as the difference between r_α and $r_{\psi*}$ tends to increase with increasing nonlinearity σ_ψ/β (Fig. 10b).

Two of the numerical solutions satisfy both an amplitude criterion and an autocorrelation criterion: both have nonlinearity measure σ_ψ/β within 5% of the respective target value and both have empirical autocorrelation

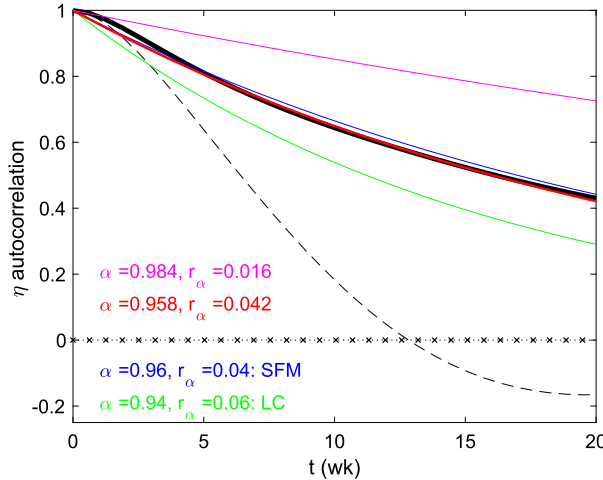


FIG. 9. Autocorrelation function $A_{0.8}(t)$ computed for the model solution with $\beta = 0.62$, $r_\psi = 0.022$, $\tau = 0.92$ along the characteristic $dx/dt = 0.8c_R$ of maximum autocorrelation (thick solid black line), and along the stationary characteristic $dx/dt = 0$ (dashed). The theoretical autocorrelation function α' for the inferred value $\alpha_{\text{eff}} = 0.958 \text{ week}^{-1}$ or $r_\alpha = 1 - \alpha_{\text{eff}} = 0.042 \text{ week}^{-1}$ is also shown (red), along with the functions α' for values $\alpha = 1 - r_\alpha$ based on the explicit model damping $r_\alpha = r_{\psi*} = UL_R^{-1}r_\psi = 0.016 \text{ week}^{-1}$ (magenta) and the stochastic model values $r_\alpha = \{0.94, 0.96\} \text{ week}^{-1}$ (green, blue) from Samelson et al. (2014, 2016). The model autocorrelation function is interpolated from domain-averaged values computed at the times marked (\times) along the t axis.

parameter α_{eff} within the previous model bounds, $0.94 < \alpha_{\text{eff}} < 0.96$ (Fig. 10). These are the two solutions with $\beta = 0.62$ and $r_\psi = 0.022$, for which $r_{\psi*} = 0.016 \text{ week}^{-1} \approx 1/62 \text{ week}^{-1}$, and either $\tau = 0.92$ or $\tau = 0.28$. For $\beta = 2.4$, the solution with $r_\psi = 0.07$, $\tau = 1$ meets the nonlinearity criterion and nearly meets the autocorrelation criterion. A few additional solutions meet or nearly meet at least one criterion, while the remainder are relatively far from meeting either.

5. Eddy statistics

Coherent eddies in the dimensional SSH field from the solution with $\beta = 0.62$, $r_\psi = 0.022$, and $\tau = 0.92$, which met both the amplitude and the autocorrelation criteria, were identified and tracked using the Chelton et al. (2011b) SSH-based procedure, after conversion of ψ to dimensional SSH η_* using the 35°N latitude scaling given in section 3 for the $\beta \approx 0.62$ set of simulations. For comparison with these midlatitude simulations, observed eddy statistics were computed from a restricted eddy dataset consisting of only those altimeter-tracked eddies that remained strictly between 20° and 40°N , or between 20° and 40°S , for their entire lifetimes. The basic structure of the mean normalized eddy amplitude, length scale, and rotational-speed life cycles found in the

observations by Samelson et al. (2014) and reproduced in the semiempirical stochastic models of Samelson et al. (2014, 2016) is found also in these $\beta \approx 0.62$ simulations and in the restricted midlatitude observed-eddy dataset: symmetry under time-reversal, negative curvature with respect to t throughout the cycles, and near-universality over the lifetime range from 16 to 80 weeks (Figs. 11a,b, 12a,b, 13a,b). The cycle-mean model dimensional amplitude and rotational speed increase with lifetime in a manner that is roughly consistent with the observed distributions for lifetimes up to half a year, but continue to increase for longer lifetimes, for which the observed scales are roughly constant, so that the model overestimates the amplitudes and speeds of the longer-lived eddies (Figs. 11c, 13c). The cycle-mean model dimensional length scale tends to modestly underestimate the observed length scale, except for lifetimes longer than a year (Fig. 12c). The model innovations—the first differences of the corresponding quantities during the eddy life cycles—have distributions that are similar to but systematically less normal than the observed innovation distributions, with smaller standard deviations and larger kurtoses (Figs. 11d, 12d, 13d).

The structure of the simulated eddy number distribution versus lifetime is generally similar to that of the observed distribution: there are many more short-lived eddies than long-lived eddies, with a power-law dependence of number on lifetime for all but the longest lifetimes (Figs. 14a,b). There are 1781 model eddies with lifetimes longer than 16 weeks, roughly 1/12 of the observed midlatitude number, with the difference arising primarily because the tiled model eddy-tracking domain area is an order of magnitude smaller than the midlatitude ocean area. At the longest lifetimes, the relatively small number of model eddies limits the statistical reliability of the estimated number distribution, but the latter nonetheless appears qualitatively consistent with the exponential dependence found in the observations. Relative to the observed distribution, however, the model eddy distribution is biased toward long eddy lifetimes, with a smaller fraction of model eddies having shorter lifetime and a larger fraction having longer lifetime. The restricted midlatitude observed-eddy statistics show a similar tendency relative to the global observed-eddy statistics, so the model distribution matches the observed midlatitude distribution better than the observed global distribution (Figs. 14a,b). A bias toward long eddy lifetimes was found for all the simulations for which the eddy analysis was performed, and may be a consequence of the single-active-layer formulation, which excludes baroclinic instability processes that might otherwise lead to more frequent decay of eddy structures. Another possible contributor to this

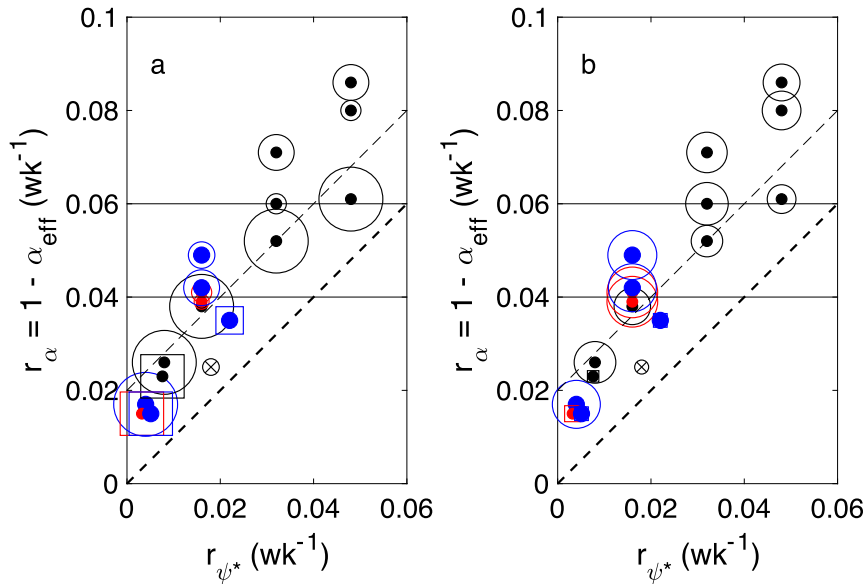


FIG. 10. Empirical autocorrelation parameter $r_\alpha = 1 - \alpha_{\text{eff}}$ (wk^{-1}) vs dimensional model damping parameter $r_{\psi^*} = UL_R^{-1} r_\psi$ for simulations as in Fig. 5, with open circle and open square size proportional to (a) $\tau^{1/4}$ and (b) nonlinearity measure σ_ψ/β . The range $0.94 \leq r_\alpha \leq 0.96$ (solid lines) of estimates from midlatitude observations, the relation $r_\alpha = r_{\psi^*}$ (thick dashed) satisfied by the linear stochastic models of Samelson et al. (2014, 2016), and the relation $r_\alpha = r_{\psi^*} + 0.02 \text{ week}^{-1}$ (thin dashed) are indicated.

discrepancy is the effect of SSH mapping errors on the identification and tracking of observed eddies.

For the $\beta = 0.62$, $r_\psi = 0.022$, $\tau = 0.92$ simulation, the distributions of amplitudes, length scales, and rotational speeds for all eddy realizations for eddies with lifetimes of 16 weeks or longer roughly reproduce the observed distributions, with the rotational-speed distribution showing the largest differences (Fig. 15). The fraction of eddies with moderate (8–15 cm) amplitudes is modestly overestimated, while the fraction of eddies with relatively small or large amplitudes is underestimated. The distribution of model eddy length scales is more sharply peaked near 70 km than is the observed distribution, and the model produces no eddies with length scales larger than 180 km. The distribution of model eddy rotational speeds is approximately symmetric around a mean of roughly 0.2 m s^{-1} , in notable contrast to the observed rotational speed distribution, which is approximately lognormal with a peak near 0.1 m s^{-1} .

The eddy number distributions versus lifetime change only modestly for solutions with the stochastic forcing time scale increased or decreased by a factor of 10, with the shorter forcing time scale resulting in a slight increase in the relative number of short-lifetime eddies, and the longer forcing time scale having the opposite effect, with similar magnitude (Figs. 14c,d). The mean life cycle statistics are likewise only modestly changed, with the fit to observations improving slightly for the

shorter forcing time scale. The amplitude and rotational speed distributions are more substantially affected, with the amplitude distribution for the longer forcing time scale, $\tau = 9.3$, closely matching the observed distribution for amplitudes less than 20 cm, and the rotational speed distribution for $\tau = 9.3$ also shifting closer to the observed distribution (Figs. 15a,c,e). In contrast, when the forcing time scale is decreased to $\tau = 0.093$, the amplitude and rotational speed distributions both shift farther from the observed distributions. The length scale distributions are relatively insensitive to these changes in τ , with a slight shift toward smaller scales for the larger τ and toward larger scales for the smaller τ . Note that for this larger- τ solution with $\beta = 0.62$, the damping parameter r_ψ has been reduced by a factor of 4, in order that the amplitude target still be matched (Fig. 8). This reduced friction results in an excessively large autocorrelation scale $\alpha_{\text{eff}} = 0.983$, $r_\alpha = 1 - \alpha_{\text{eff}} = 0.017$ (Fig. 10). Thus, while this solution meets the amplitude criterion and matches the overall eddy amplitude, length scale, and rotational speed statistics better than the smaller τ solution, it does not meet the autocorrelation criterion, and it exaggerates the bias toward long lifetimes in the eddy number distribution. Consequently, the selection of a single optimal solution among this set would depend strongly on the relative importance ascribed to the various criteria and comparisons.

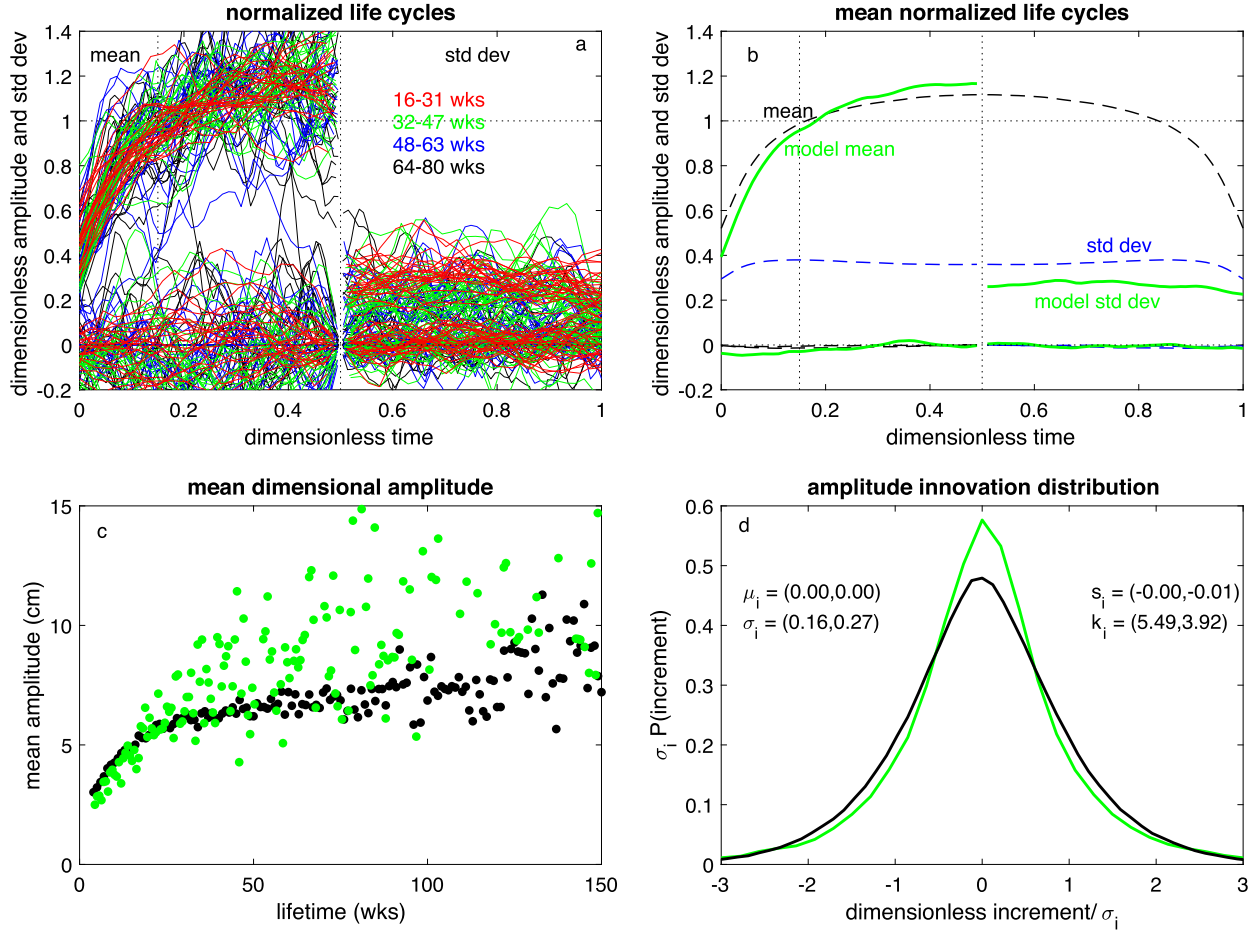


FIG. 11. Normalized eddy amplitude life cycles for solution with $\beta = 0.62$, $r_\phi = 0.022$, $\tau = 0.92$. (a) Mean life cycles vs normalized time for each lifetime class with lifetime between 16 and 80 weeks. (b) Mean life cycle for all eddies with lifetimes between 16 and 80 weeks. The mean and standard deviation life cycles (labeled) are shown for the model (green solid lines) and midlatitude observations (black and blue dashed), with the model mean and standard deviation shown separately over the subintervals with normalized time $t < 0.5$ and $t > 0.5$. The symmetric and antisymmetric parts under time reversal are shown separately, with all of the antisymmetric parts being negligibly small relative to the symmetric parts. (c) Mean dimensional amplitude vs eddy lifetime for the model (green) and midlatitude observations (black), for eddies with lifetimes of at least 4 weeks. (d) Normalized distributions of innovations (first differences in time) for the normalized eddy life cycles for all model (green) and midlatitude observed (black) eddies with lifetimes of at least 16 weeks, with mean, standard deviation, skewness, and kurtosis of the (model, observed) distributions as shown.

In summary, changing the forcing time scale has mixed effects on the eddy statistics. Lengthening it so that $\tau \gg 1$, while decreasing the damping to maintain the amplitude, gives a substantially improved match to the observed amplitude and rotational speed distributions, has a mixed effect on the mean life cycle statistics, and slightly increases the bias toward long-lifetime eddies; the reduced damping, however, increases the autocorrelation scale α_{eff} to values larger than observed. Shortening it so that $\tau \ll 1$ slightly reduces the bias toward long-lifetime eddies, and fits amplitude, length scale, and speed life cycles and mean amplitude versus lifetime slightly better, but increases the mismatch in mean eddy speed versus

lifetime and in the eddy amplitude, length scale, and speed distributions.

The eddy statistics for the more moderately nonlinear solutions, with $\beta = 2.4$, $\phi = 24^\circ$, and $L_R = 60$ km, show much greater differences from the observed statistics. Perhaps surprisingly, the corresponding eddy number distributions versus lifetime are even more biased toward long lifetimes than the more strongly nonlinear solutions, although there is some hint that they may better represent the transition to exponential structure of the long-lifetime distribution (Figs. 14e,f). The eddy amplitudes and rotational speeds for the moderately nonlinear solutions are generally much smaller, and the length scales much larger, than observed, though again

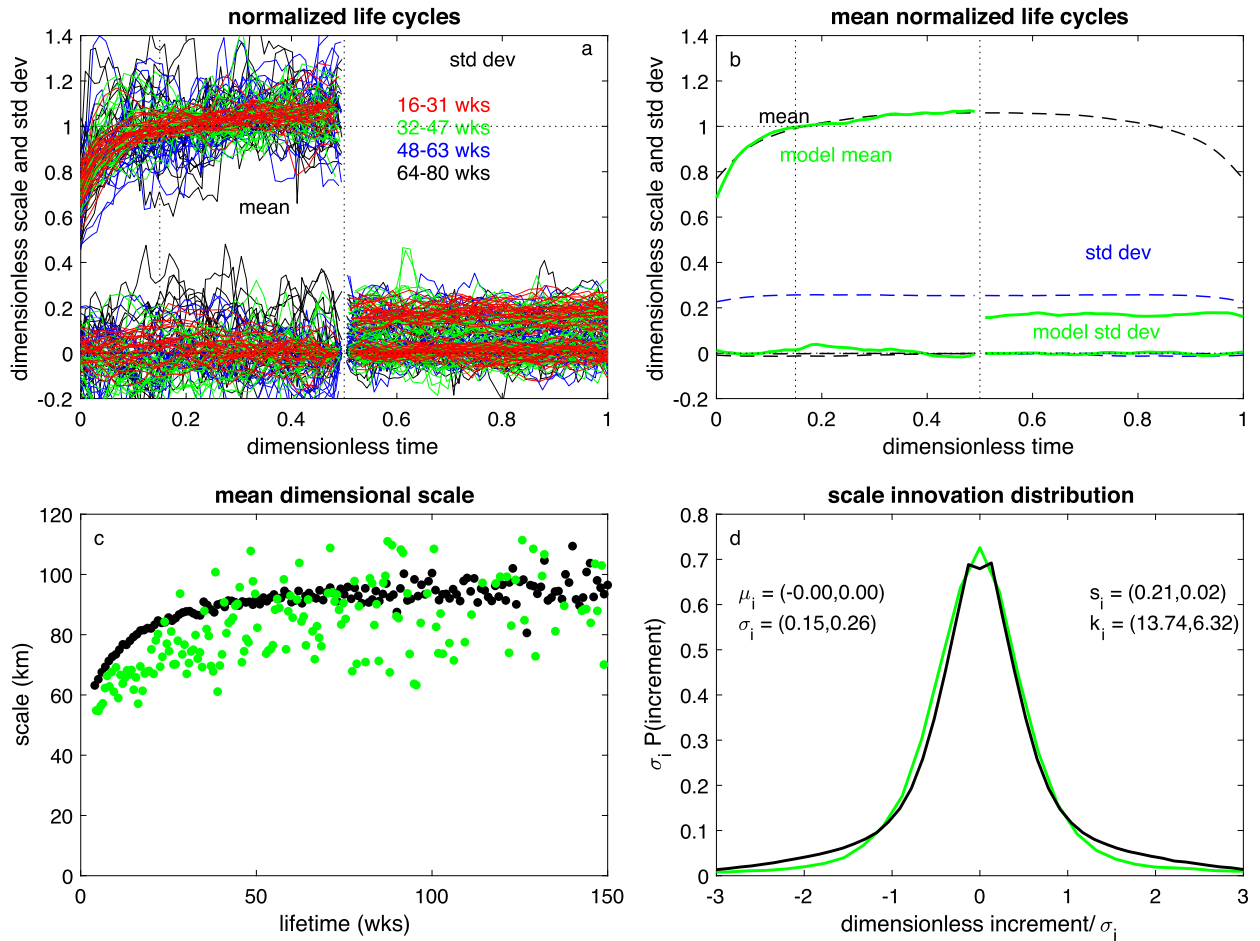


FIG. 12. As in Fig. 11, but for normalized eddy length scale life cycles.

the model produces no eddies with length scales larger than 180 km (Figs. 15b,d,f). The primary focus of the subsequent analysis is therefore on the more strongly nonlinear solutions with $\beta \approx 0.6$. It should be noted, however, that the $\beta = 2.4$ solutions may be more relevant for comparison to observations in the tropics, within approximately 20° latitude of the equator.

6. Spectral description

The advective nonlinearity for all solutions with $\beta \approx 0.6$ spreads the model SSH spectral power over total wavenumber K from the stochastic forcing band near the deformation radius $K = 1$ to higher and lower wavenumbers, with the high-wavenumber spectrum following a K^{-5} power law, consistent with the classical theory of geostrophic turbulence (Fig. 16). Of the three solutions with $\beta = 0.62$ for which the eddy statistics were analyzed, the two with $r_\psi = 0.022$, and $\tau < 1$ have very similar total-wavenumber SSH power spectra, while the third, with $\tau = 9.3$ and $r_\psi = 0.0054$, has relatively more

power at wavenumbers $K < 0.5$ and less power at wavenumbers $K > 0.5$ (Fig. 16). The spectral shape of this third solution, with longer stochastic forcing time scale and weaker damping, appears to match that of the observed mean AVISO radial wavenumber spectrum slightly better than the other two for $0.3 \leq K \leq 0.7$, that is, for scales roughly 1.5–3 times larger than the deformation radius wavelength (Fig. 16).

For the model solution with $\beta = 0.62$, $r_\psi = 0.022$, and $\tau = 0.92$, the zonal wavenumber–frequency power spectrum of the dimensionless streamfunction or, equivalently, SSH (Fig. 17a) shows a nondispersive structure that is very similar to observed wavenumber–frequency spectra (e.g., Fig. 2a), with effective phase speed near the linear long-wave speed, and with both an apparent absence of short-wave dispersion and rapidly declining spectral power for wavenumbers with magnitudes near and greater than the deformation radius wavenumber. Kinetic energy spectra show the same nondispersive structure (see appendix, Fig. A1). Some subtle differences in the spectral structure may be noted

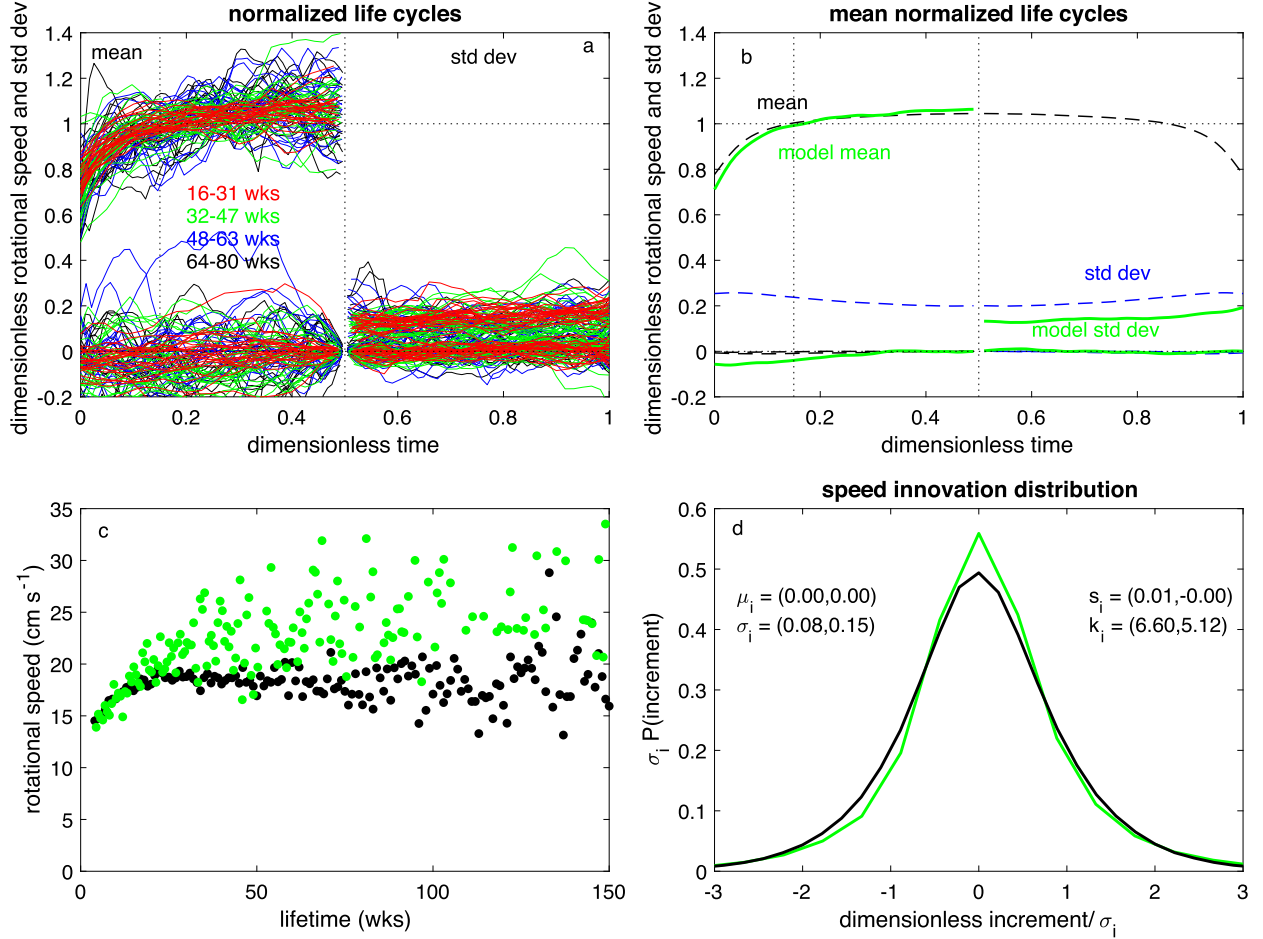


FIG. 13. As in Fig. 11, but for normalized eddy rotational speed life cycles.

away from the nondispersive line: for spectral power levels two or more orders of magnitude smaller than the maximum, the observed spectra tend to have isolines of constant spectral power that are roughly parallel to the nondispersive line, while the model spectra tend to have constant-power isolines that are roughly parallel to lines of constant zonal wavenumber. The other solutions with $\beta \approx 0.6$ have similar wavenumber-frequency spectra, with similar subtle differences from the observed spectrum.

An alternate representation of the same wavenumber-frequency spectral information is available that more directly illustrates the influence of the nonlinearity. If the nonlinear term in (7) is moved to the right-hand side, the Fourier transform of the resulting equation is taken, and the power spectrum is then formed, the result is:

$$\mathcal{L}^{-1} |\hat{\psi}|^2 = |\hat{\mathcal{F}} - \hat{J}|^2, \quad (22)$$

where \mathcal{L} is the transfer function defined by

$$\mathcal{L} = \{[\omega(K^2 + 1) + \beta k]^2 + r^2\}^{-1}, \quad (23)$$

\hat{J} is the Fourier transform of $J(\psi, \nabla^2 \psi)$ and for simplicity the enstrophy dissipation term $\hat{\mathcal{D}}_{\text{ens}}$, which is negligible in the SSH dynamical balance, has been dropped. If (7) were linear, so that $\hat{J} = 0$, and the forcing were known, then the transfer function \mathcal{L} would give the power spectrum of the solution directly,

$$|\hat{\psi}|^2 = \mathcal{L} |\hat{\mathcal{F}}|^2. \quad (24)$$

Conversely, if the solution spectrum $\hat{\psi}$ were known in the linear case, then the corresponding forcing spectrum could be obtained directly from (22) with $\hat{J} = 0$:

$$|\hat{\mathcal{F}}|^2 = \mathcal{L}^{-1} |\hat{\psi}|^2. \quad (25)$$

For linear simulations conducted using the same numerical scheme as for the full form of (7) but with the nonlinear term neglected, this reconstruction (25) of the power spectrum of the forcing from that of the solution

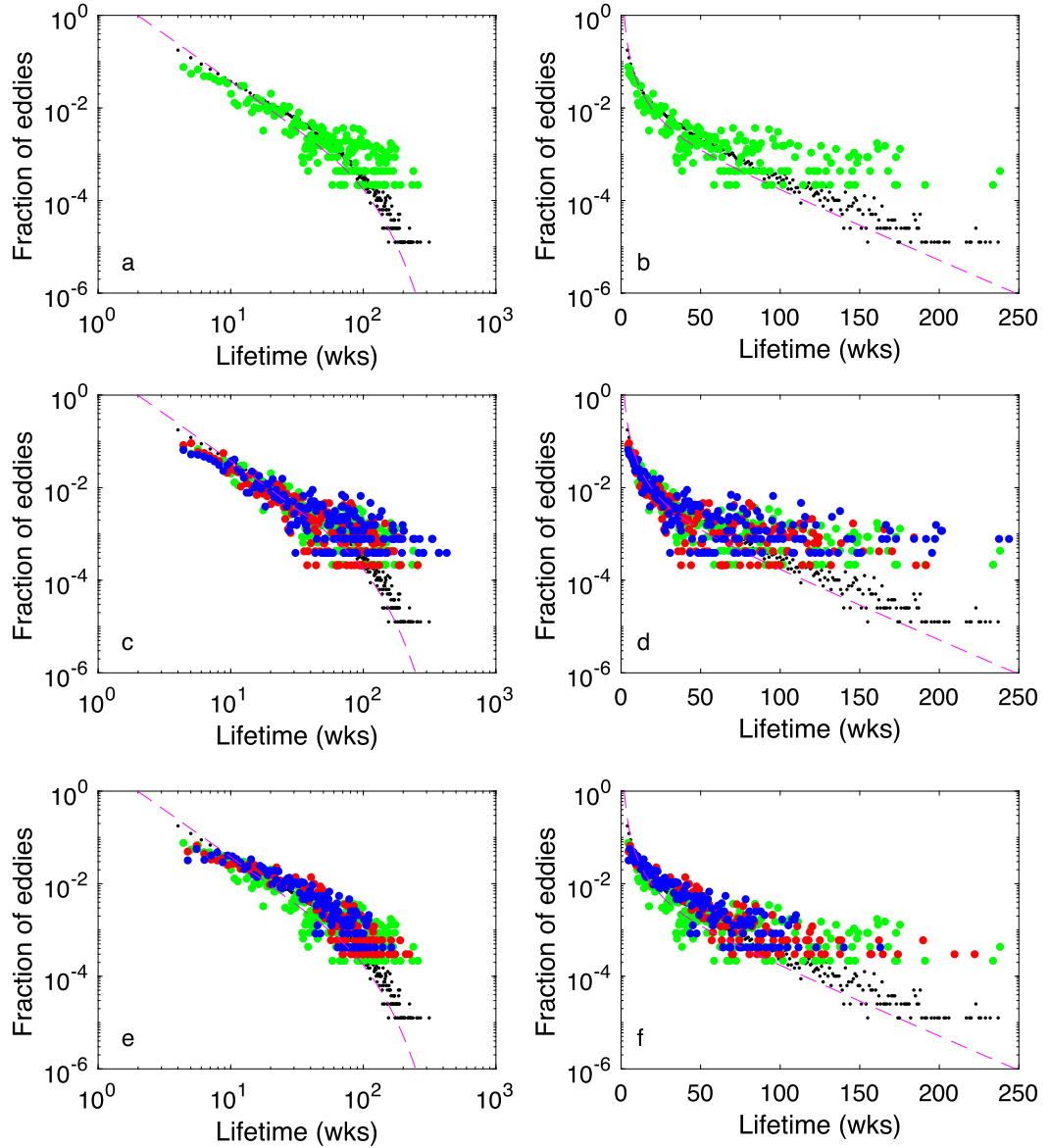


FIG. 14. Tracked-eddy number distributions vs lifetime (weeks) on (a),(c),(e) log–log and (b),(d),(f) log–linear axes for the model solutions with (a)–(f) $\beta = 0.62$, $r_\psi = 0.022$, $\tau = 0.92$ (green dots); also shown in (c) and (d) are $\beta = 0.62$, $r_\psi = 0.022$, $\tau = 0.093$ (red), $\beta = 0.61$, $r_\psi = 0.0054$, $\tau = 9.3$ (blue); and in (e) and (f) $\beta = 2.4$, $r_\psi = 0.07$, $\tau = 1$ (red), $\beta = 2.4$, $r_\psi = 0.01$, $\tau = 5$ (blue). The distribution for the midlatitude AVISO observations is shown in each panel (black dots), along with the analytical function fit by Samelson et al. (2016) to the observed global-mean distribution (dashed magenta line).

is accurate (Fig. 18). For the nonlinear numerical simulations, the power spectrum $\mathcal{L}^{-1}|\hat{\psi}|^2$ in (22) computed from the solution can be compared to the power spectrum $|\hat{\mathcal{T}}|^2$ of the forcing, and any differences between these two spectra can be attributed to the nonlinearity $J(\psi, \nabla^2\psi)$ in (7). This gives a direct illustration of the influence of the nonlinearity on the spectral structure.

For the nonlinear model solutions with $\beta = 0.62$, the inverted zonal wavenumber–frequency power spectrum

$\mathcal{L}^{-1}|\hat{\psi}|^2(k, \omega)$ shows two distinct effects of the nonlinearity (Figs. 17, 19). First, there is a dramatic reduction in power of the inverted spectrum around the linear inviscid dispersion relation, $\omega = -\beta k/(K^2 + 1)$, which contrasts sharply with the symmetric wavenumber dependence of the forcing (Fig. 18). Second, away from the linear dispersion relation the spectral power is spread beyond the interval of forcing wavenumbers to much larger wavenumbers, with the wavenumber range

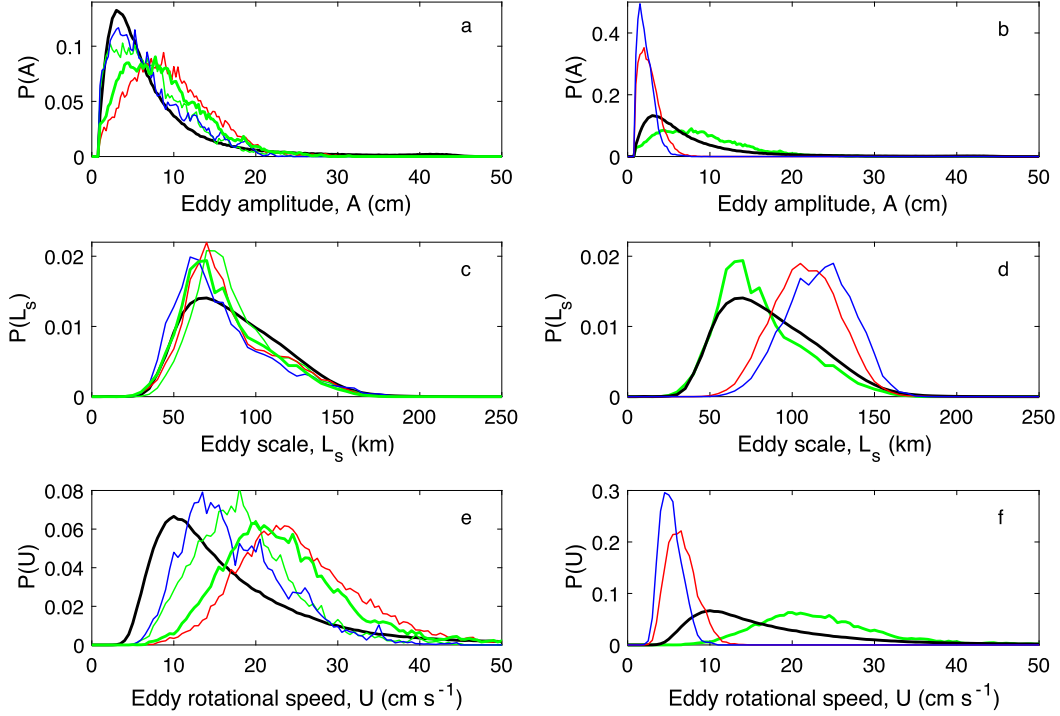


FIG. 15. Probability distributions of (a),(b) eddy amplitudes, (c),(d) length scales, and (e),(f) rotational speeds for the solutions with $\beta = 0.62$, $r_\psi = 0.022$, $\tau = 0.92$ (thick green line) in (a)–(f); (a),(c),(e) $\beta = 0.62$, $r_\psi = 0.022$, $\tau = 0.093$ (red), $\beta = 0.62$, $r_\psi = 0.0054$, $\tau = 9.3$ (blue), and $\beta = 0.62$, $r_\psi = 0.022$, $\tau = 0.92$ with space-time smoothing (thin green); and (b),(d),(f) $\beta = 2.4$, $r_\psi = 0.07$, $\tau = 1$ (red), and $\beta = 2.4$, $r_\psi = 0.01$, $\tau = 5$ (blue). The distributions for the midlatitude AVISO observations are also shown (black).

tending to increase with frequency, and to larger frequencies (Fig. 19). Thus, at statistical equilibrium, the nonlinearity removes energy from the resonant linear wave field and scatters it to other wavenumbers and frequencies. For all wavenumbers $|k| > 1$, outside the range of the forcing, there is a net input of energy from the nonlinearity, but along the dispersion relation this input is much reduced relative to its magnitude at higher and lower frequencies for the same wavenumber $k < 0$, and at similar frequencies for the corresponding positive wavenumber $|k|$ (Fig. 19c). The reduction in power around the dispersion relation is most dramatic at wavenumbers $k < -0.5$, corresponding to scales smaller than twice the deformation radius wavelength, but is still discernible at even larger scales, in the wavenumber range $-0.5 \leq k < 0$ (Fig. 17b).

For the observed SSH zonal wavenumber-frequency power spectrum from the gridded AVISO data along 35°S, an analogous inversion $\mathcal{L}_*^{-1} |\hat{\eta}_*|^2$ can be computed (Fig. 2b). For simplicity, and to avoid additional dependence on the degree of mismatch between the various theoretical linear dispersion relations and the observed SSH spectrum, an empirical dispersion relation was constructed from the observed spectrum, with the form

$$\omega_* = -c_* k_*/(\lambda_*^2 k_*^2 + 1), \quad (26)$$

where c_* is an effective long-wave speed, λ_* is an effective deformation-radius wavelength, and k_* is the dimensional zonal wavenumber. Any effect of meridional structure was incorporated only implicitly through the fit of the empirical parameters. The empirical inverse transfer function was then constructed from this empirical dispersion relation, taking the form

$$\mathcal{L}_*^{-1} = \{\omega_* [k_*^2 + (2\pi/\lambda_*)^2] + \beta k_*\}^2 + r_*^2, \quad (27)$$

where $r_* = 1/16 \text{ week}^{-1}$ is an estimated empirical damping rate that was deliberately chosen to be relatively large, in order not to underestimate the minimum of \mathcal{L}_*^{-1} along the dispersion relation, which would result in an overestimate of the effect of the nonlinearity.

The structure of the resulting inverted spectrum $\mathcal{L}_*^{-1} |\hat{\eta}_*|^2$ (Fig. 2b) is strikingly similar to the inverted model spectrum $\mathcal{L}_*^{-1} |\hat{\psi}|^2(k, \omega)$ (Fig. 17b). Most notably, the local minimum in power along the empirical dispersion relation is well defined and very similar to that in the model spectrum. The minimum in the observed inverted spectrum is clearly evident for all zonal

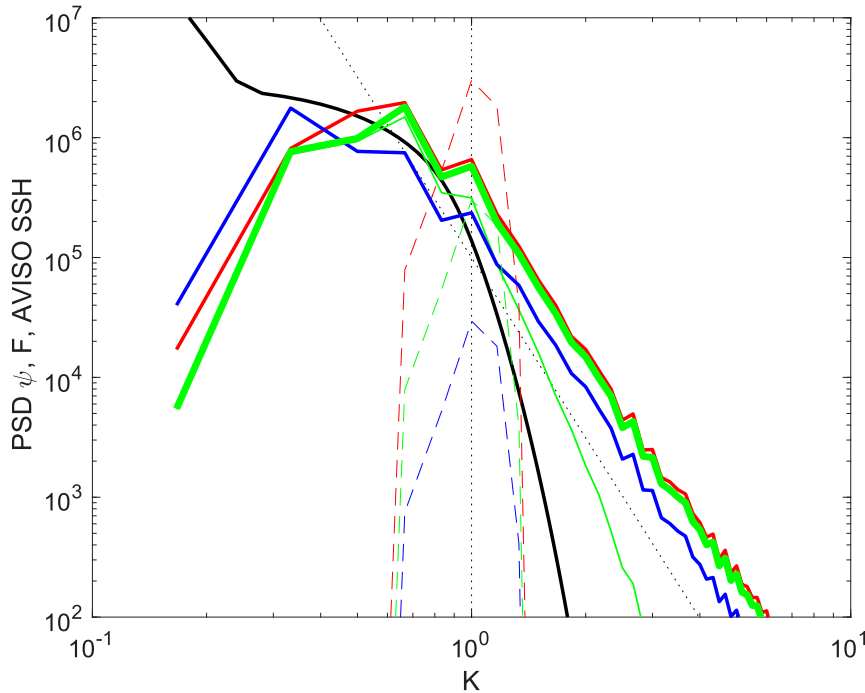


FIG. 16. Power spectra of dimensionless model streamfunction ψ or sea surface height η (solid) and stochastic forcing \mathcal{F} (dashed) vs dimensionless wavenumber magnitude K from simulations with $\beta = 0.62$, $r_\psi = 0.022$, $\tau = 0.093$ (red); $\beta = 0.62$, $r_\psi = 0.022$, $\tau = 0.92$ (thick green); and $\beta = 0.61$, $r_\psi = 0.0054$, $\tau = 9.3$ (blue). The power spectrum for the space-time smoothed solution with $\beta = 0.62$, $r_\psi = 0.022$, $\tau = 0.92$ (thin green) is also shown, along with the approximate AVISO SSH wavenumber-magnitude spectrum (solid black) used by Samelson et al. (2016) to constrain the wavenumber structure of the linear stochastic field model, and the dimensionless deformation-radius wavenumber $K = 1$ and a K^{-5} power-law slope (dotted black).

wavenumbers $k_* < -2 \times 10^{-3}$ cpkm and so extends to wavelengths as large as 500 km, which are much larger than the approximately 200-km wavelength resolution limit of the gridded AVISO data (Chelton et al. 2011b). This is strong evidence that nonlinearity controls the structure of the wavenumber-frequency spectrum of SSH in the ocean mesoscale regime. This result has been previously suggested on the basis of the nondispersing structure of the SSH power spectrum (e.g., Chelton et al. 2011a; Early et al. 2011; Berloff and Kamenkovich 2013; Morten et al. 2017; LaCasce 2017), but the rapid decline in spectral power toward higher wavenumbers has been difficult to separate from the decline in power associated with the approach to the spatial resolution limit of the AVISO data, and consequently it has been difficult to attribute the structure of the power spectrum in this range unambiguously to nonlinear effects. Although based on the same spectral information, the representation in terms of the inverted power spectrum (22) illustrates more clearly and definitively that a dramatic effect of nonlinearity on the wavenumber-frequency spectrum is resolved by the gridded altimeter data.

The inverted model spectrum $\mathcal{L}^{-1} |\hat{\psi}|^2(k, \omega)$ illustrates that the spreading of energy by the nonlinearity extends continuously in the model to the highest frequencies and smallest spatial scales, with the nonlinear removal of energy from the linear dispersive wave line extending also to the smallest spatial scales (Fig. 19c). The structure of this inverted spectrum is dramatically different from the forcing spectrum, revealing the broad influence of nonlinearity. The structure is not strongly dependent on the time scale of the forcing, except to the extent that the signature of the high-frequency forcing can be recognized in the inverted power spectra for the solutions with small stochastic time scales. From comparisons of the power spectra and inverted power spectra, there is not a clear best match to the observed 35°S Indian Ocean spectra (Fig. 2) among the $\beta \approx 0.6$ solutions, although the structure of the power spectrum for $k > 0$ may suggest a preference for the $\tau = 9.3$ solution among the three for which the eddy statistics were computed.

A broader perspective on the wavenumber-frequency spectral structure of the observed SSH field is provided by a set of 16 spectra $|\hat{\eta}_*|^2(k_*, \omega_*)$ computed from the

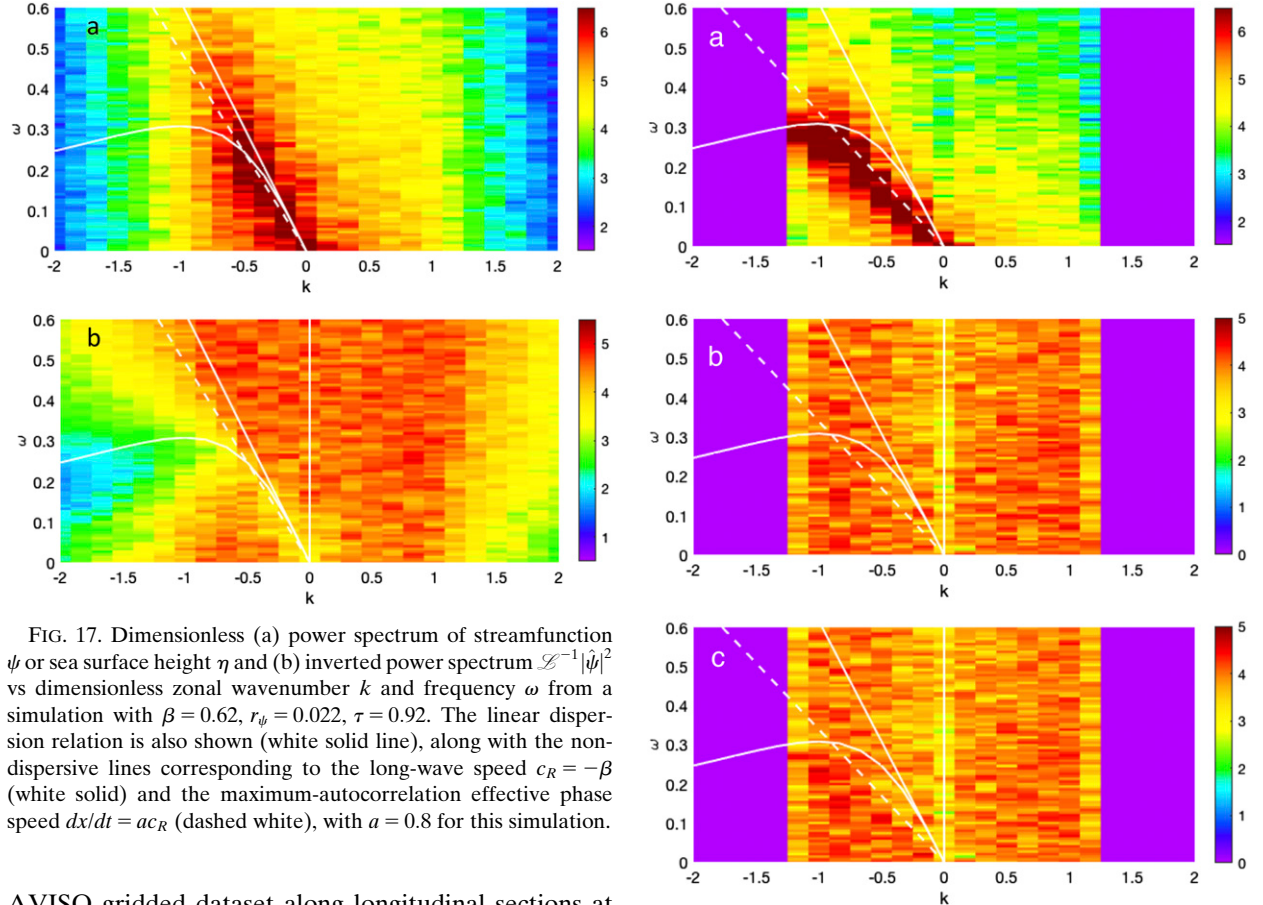


FIG. 17. Dimensionless (a) power spectrum of streamfunction ψ or sea surface height η and (b) inverted power spectrum $\mathcal{L}^{-1}|\hat{\psi}|^2$ vs dimensionless zonal wavenumber k and frequency ω from a simulation with $\beta = 0.62$, $r_\psi = 0.022$, $\tau = 0.92$. The linear dispersion relation is also shown (white solid line), along with the non-dispersive lines corresponding to the long-wave speed $c_R = -\beta$ (white solid) and the maximum-autocorrelation effective phase speed $dx/dt = ac_R$ (dashed white), with $a = 0.8$ for this simulation.

AVISO gridded dataset along longitudinal sections at various locations, for frequencies extending to the 1/14 cpd Nyquist frequency and zonal wavenumbers extending to 16×10^{-3} cpkm, or wavelengths of 62 km, much smaller than the nominal 200-km spatial resolution limit of the dataset (Fig. 20). This set includes the 35°S spectrum discussed above (Fig. 2). The locations for these spectra were selected to avoid western boundary current extensions and the Antarctic Circumpolar Current, where advection by mean currents strongly modifies the spectral structure. Viewed from this perspective, all of the 16 spectra have similar qualitative structure: a maximum along a nondispersing line corresponding to westward propagation, at an effective phase speed that is typically within a factor of 2 of theoretical long-wave phase speeds for the corresponding region, and a decay in spectral level toward higher frequencies and away from the fixed-frequency maximum toward higher wavenumber magnitudes.

The corresponding set of 16 inverted power spectra (again including the 35°S spectrum shown in Fig. 2), computed as $\mathcal{L}_*^{-1}|\hat{\eta}_*|^2$ for transfer functions from empirical dispersion relations estimated individually for each spectrum, show a similarly consistent, but more complex, structure (Fig. 21). In each, there is a reduced

FIG. 18. Power spectrum of dimensionless (a) streamfunction ψ or sea surface height η , (b) stochastic forcing \mathcal{F} , and (c) inverted power spectrum $\mathcal{L}^{-1}|\hat{\psi}|^2$ vs dimensionless zonal wavenumber k and frequency ω from a linear simulation with $\beta = 0.62$, $r_\psi = 0.022$, $\tau = 0.92$. Dispersion relation and nondispersing lines are as in Fig. 17, with $a = 0.55$ for the maximum-autocorrelation characteristic.

spectral level along the empirical dispersion relation, consistent with the removal of energy from the linear wave field by nonlinearity. In addition, there are two other consistent features, at higher frequencies, with no immediate physical interpretation: a maximum centered along the nondispersing line, and a second feature consisting of twin, parallel lobes of variance centered near $k = \pm 5 \times 10^{-3}$ cpkm and increasing toward the Nyquist frequency. The maxima along the nondispersing line extend to high frequency, generally terminating either at the spatial resolution limit, for the higher latitudes where the nondispersing propagation is slower, or at the Nyquist frequency, for the lower latitudes where the nondispersing propagation is faster. Both of these features extend continuously into frequencies and wavenumbers well beyond the nominal 30-day temporal and 200-km spatial resolution limits of the AVISO gridded

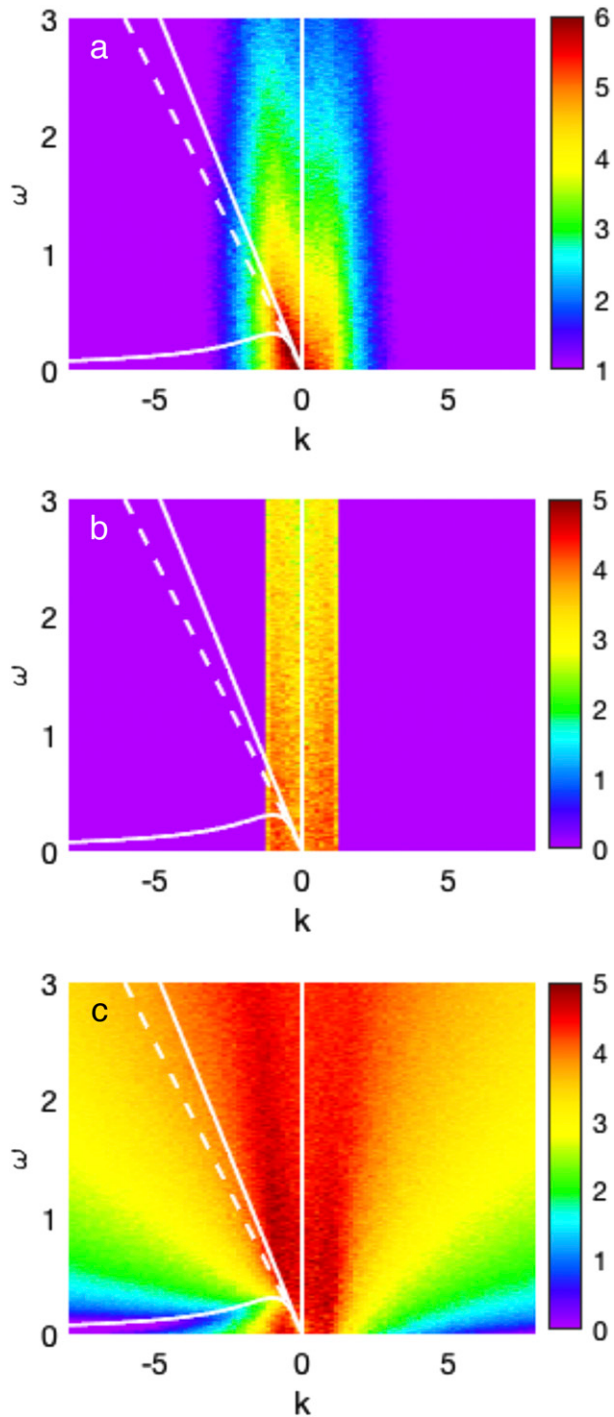


FIG. 19. Power spectrum of dimensionless (a) streamfunction ψ or sea surface height η , (b) stochastic forcing \mathcal{F} , and (c) inverted power spectrum $\mathcal{L}^{-1}|\psi|^2$ vs dimensionless zonal wavenumber k and frequency ω from the simulation with $\beta = 0.62$, $r_\psi = 0.022$, $\tau = 0.92$. Dispersion relation and nondispersive lines are as in Fig. 17.

dataset, and thus may in part reflect characteristics of the data processing procedures used to produce the merged dataset from the along-track altimeter data.

The reduced spectral level along the dispersion relation is reproduced by the inverted power spectra for the model solutions (Figs. 17b, 19c). However, the two additional high-frequency features of the inverted power spectra of observed SSH are not recognizably reproduced by the model solutions. The model inverted power spectra generally lack a maximum along the nondispersive line at high frequencies (Fig. 19c). The model high-frequency spectral structure is more similar to the second feature, with its symmetry in positive and negative wavenumber at fixed frequency, but generally tends to decay toward higher frequency, in contrast to the symmetric spectral lobes in the observed spectra, which tend to increase in amplitude toward higher frequency.

7. Space-time filtering

A high-frequency maximum along the nondispersive line in the inverted power spectrum, which is present in the observed spectra (Fig. 21) but absent from the model spectra (Fig. 19c), can be reproduced by the model if the model output is smoothed with a moving space-time filter prior to the spectral analysis (Figs. 22a,b). The filter characteristics for this smoothing are chosen (see appendix) to be relatively consistent with basic aspects of the data processing used to produce the AVISO merged, gridded dataset (Fig. 22). This result is consistent, in a general sense, with previous studies showing that the correspondence between results obtained from numerical models and from AVISO gridded observations sometimes improves if the model results are smoothed (Arbic et al. 2013).

The second high-frequency feature found in the observed inverted spectra (Fig. 21), the twin lobes of variance centered near $k = \pm 5 \times 10^{-3}$ cpkm, are not reproduced by the spectra of the moving space-time filtered model output (Figs. 22a,b). However, the filtered output for the case $\beta = 0.62$, $r_\psi = 0.022$, $\tau = 0.92$ does better reproduce the slope of the low-power isolines in the observed spectra: for the observations and the filtered power spectra, these isolines are roughly parallel to the nondispersive line even for $k > 0$ (Figs. 2a, 22a), while for the unfiltered power spectra, these isolines are roughly independent of frequency for $k > 0$ (Fig. 17a). The filtered output also more closely resembles the AVISO total wavenumber power spectrum, with reduced power and steeper decay for wavenumbers $K > 1$ (Fig. 16).

The eddy analysis was also conducted on the filtered model output for this case. The resulting distributions of eddy amplitude and rotational speed are in better

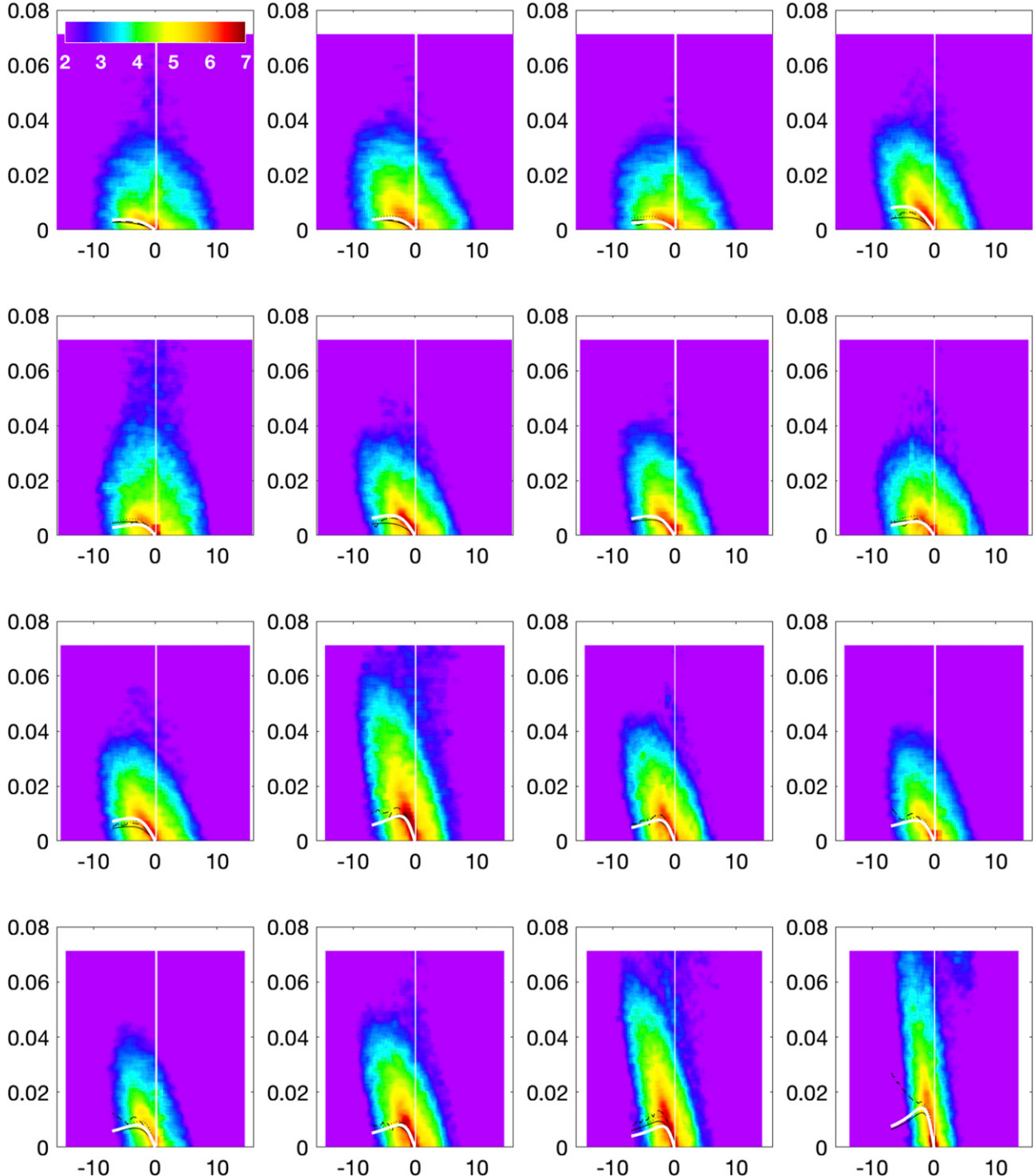


FIG. 20. Power spectra of SSH variability ($\text{cm}^2 \text{cpd}^{-1} \text{cpkm}^{-1}$) computed from the AVISO gridded dataset vs zonal wavenumber (10^{-3}cpkm) and frequency (cpd). The maximum frequency is the 1/14 cpd Nyquist frequency for the weekly dataset, and the spectra are computed from observations (from left to right) along (top) South Pacific 45°S, 150°–110°W; South Indian 40°S, 80°–110°E; South Pacific 38°S, 130°–100°W; and South Indian 35°S, 40°–85°E; (top middle) North Pacific 33°N, 180°E–130°W; South Atlantic 33°S, 50°W–0°W; North Atlantic 30°N, 70°–40°W; and South Pacific 30°S, 170°E–120°W; (bottom middle) South Indian 30°S, 60°–100°E; North Pacific 24°N, 125°–165°E; South Pacific 24°S, 160°E–135°W; and North Atlantic 24°N, 60°W–30°W; (bottom) South Atlantic 24°S, 40°–10°W; South Indian 24°S, 50°–100°E; North Pacific 21°N, 130°E–170°W; and South Indian 14°S, 70°–120°E. Dispersion relations are shown as in Fig. 2, for the parameter values listed in the appendix.

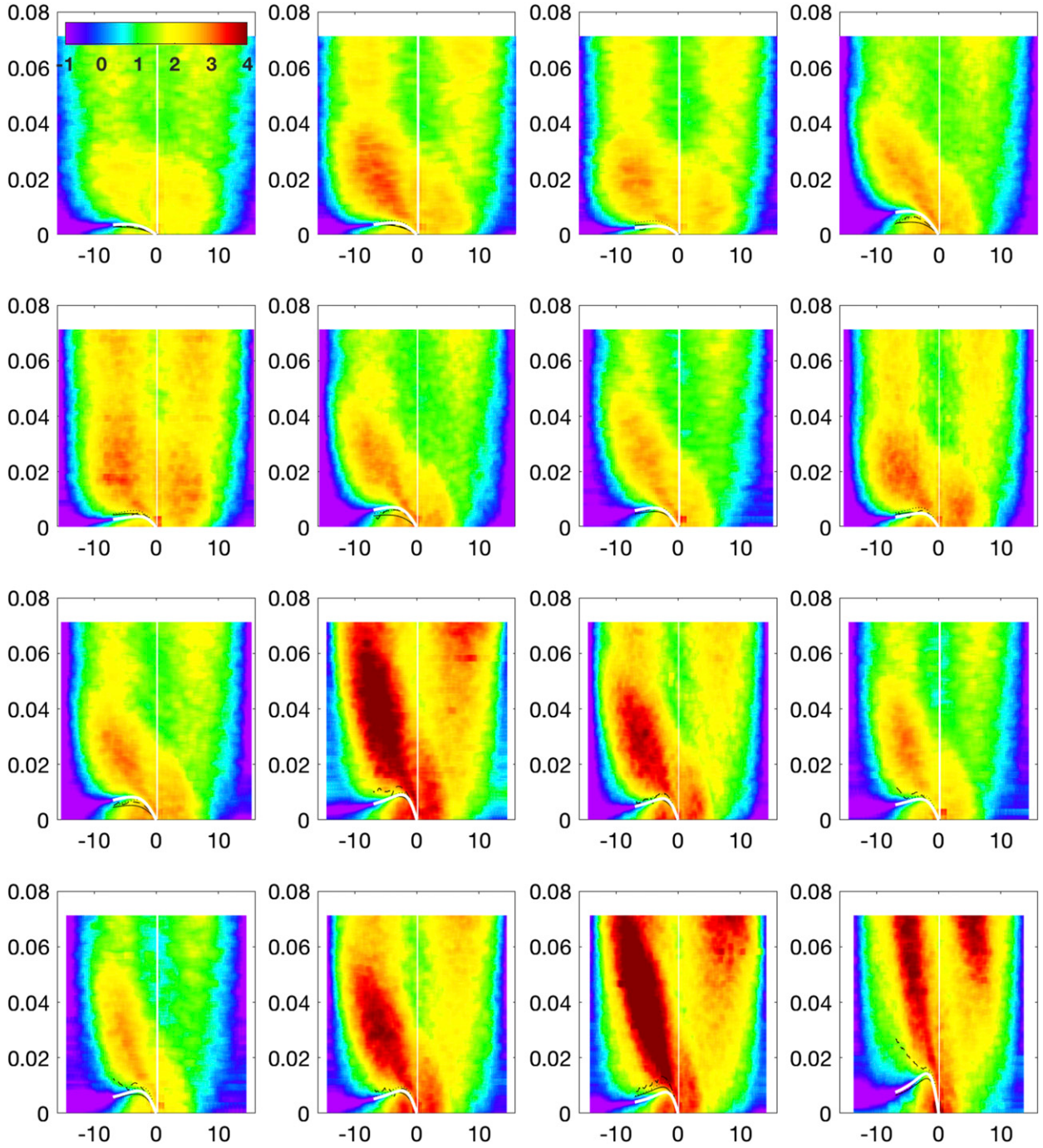


FIG. 21. As in Fig. 20, but for inverted power spectra $\mathcal{L}^{-1}|\hat{\eta}_*|^2$ of SSH variability ($\text{cm}^2 \text{week}^{-2} \text{cpd}^{-1} \text{cpkm}^{-1}$).

agreement with the observed distributions than the unfiltered model output (Figs. 15a,c,e). These distributions are also similar to those obtained in the case with the long stochastic forcing time scale, $\beta = 0.62$, $r_\psi = 0.0054$, $\tau = 9.3$. On the other hand, the simulated eddy length scale distribution, the mean normalized eddy life cycle statistics, and the autocorrelation scale from

the filtered output are in poorer agreement with the observations, with the latter two again similar to the case with the long forcing time scale but the former showing an opposite effect.

A closer resemblance to the observed linear-inverted spectral structure (Fig. 21) can be achieved if the moving space-time filtered fields are blended with fields that

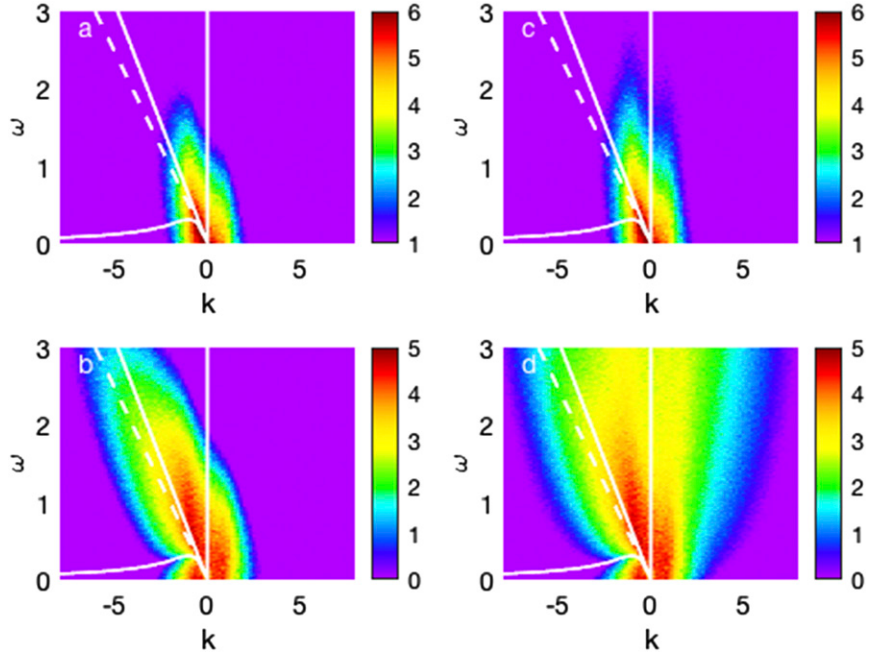


FIG. 22. Power spectrum of dimensionless (a),(c) streamfunction ψ or sea surface height η and (b),(d) inverted power spectrum $\mathcal{L}^{-1}|\hat{\psi}|^2$ vs dimensionless zonal wavenumber k and frequency ω , for the (left) space–time smoothed simulation with $\beta = 0.62$, $r_\psi = 0.022$, $\tau = 0.92$ and (right) a blended, smoothed set of model fields consisting of $0.8 \times$ the space–time smoothed fields from (a) and (b) plus $0.2 \times$ the fields from the same simulation, but with spatial smoothing only. Dispersion relation and nondispersive lines are as in Fig. 19, which shows the same model fields without smoothing.

have been smoothed only spatially. The inverted model spectrum for these blended fields from the $\beta = 0.62$, $r_\psi = 0.022$, $\tau = 0.92$ case shows structures similar to both high-frequency features in the observed spectra, including the zonal-wavenumber-symmetric parallel lobes as well as the maximum along the nondispersive line (Figs. 22c,d). In the model case, the second, parallel-lobe feature evidently reflects the stochastic forcing in the wavenumber annulus around $K = 1$. It is thus tempting to speculate that this feature in the observations may reflect an analogous physical signal of baroclinic interactions; on the other hand, there is no clear rationale for the blending, and the observed features may merely be filtered noise.

8. Spectral description for $\beta = 2.4$

The solution for $\beta = 2.4$, $r_\psi = 0.07$, and $\tau = 1$ was intended to represent a dimensional SSH standard deviation of 0.02 m near latitude 24° with internal deformation radius $L_R = 60$ km. This solution has $\sigma_\psi/\beta = 0.85$ and consequently is less nonlinear than the solutions with $\beta \approx 0.6$ and $\sigma_\psi/\beta \approx 7$. This solution has power spectrum and inverted power spectrum structure (Fig. 23) that are intermediate between the more

nonlinear $\beta \approx 0.6$ cases (Fig. 17) and the linear example for which the inverted power spectrum exactly reproduces the forcing spectrum (Fig. 18).

While some aspects of the $\beta = 2.4$ spectral structure may appear to match the observed spectra better, more detailed examination reveals further discrepancies. The low-level power isolines in the power spectrum for $k > 0$ have a slope that is roughly parallel to the line of maximum power, in perhaps better agreement with the observed low-level spectral isolines, but the amplitude decay away from the line of maximum power is more abrupt than in the observations, and the line of maximum power falls well below the long-wave speed. Similarly, although the effective damping r_α computed from autocorrelation decay scale for this solution is 0.035, not far from the target range $0.04 \leq r_\alpha \leq 0.06$, the characteristic along which this maximum autocorrelation is found has an effective speed that is only slightly more than half of the long-wave speed. These slow propagation speeds are inconsistent with the observed SSH signal propagation speeds, which are systematically no less, and typically larger, than the local theoretical long-wave speeds.

In addition, the inverted power spectrum (Fig. 23b) shows only a relatively weak reduction of power along

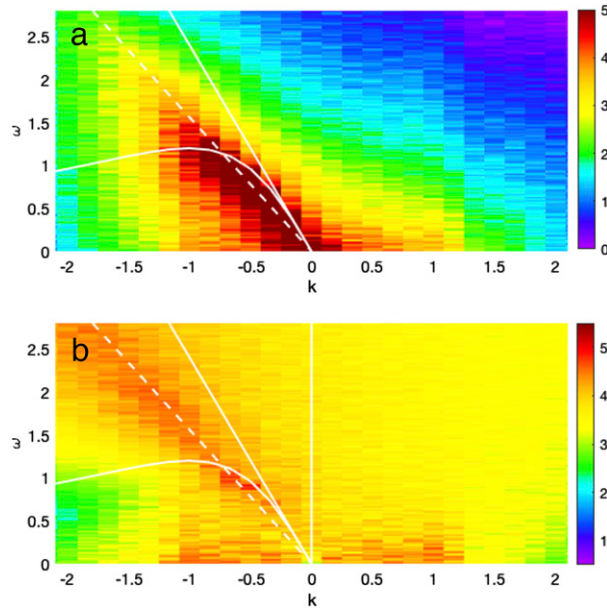


FIG. 23. Dimensionless (a) power spectrum $|\hat{\psi}|^2$ or $|\hat{\eta}|^2$ of streamfunction ψ or sea surface height η and (b) inverted power spectrum $\mathcal{L}^{-1}|\hat{\psi}|^2$ vs dimensionless zonal wavenumber k and frequency ω from the simulation with $\beta = 2.40$, $\tau = 5$, $r_\psi = 0.024$. Dispersion relation and nondispersive lines are as in Fig. 17, with $a = 0.65$ for the maximum-autocorrelation characteristic.

the dispersion relation, in contrast with the sharp reductions evident in the observed 35°S inverted power spectrum (Fig. 2b) and in those for the $\beta \approx 0.6$ solutions (Fig. 17b). There is an amplification of the inverted power spectrum that is aligned approximately along the long-wave nondispersive line—though again at a slower effective propagation speed—that bears some resemblance to the nondispersive feature in the observed inverted power spectra (Fig. 21). However, even for this more linear solution, there is broad spreading of energy at slightly lower power levels across positive and negative wavenumbers, with the wavenumber range increasing toward higher frequency. Consequently, the inverted model spectrum contains only a hint of the structure along the nondispersive line that is a dominant but unexplained feature of the observed inverted power spectra, and does not provide a persuasive physical explanation for this structure.

Comparison of this nominal latitude 24° simulation may be made, for example, with the observed SSH power spectrum along 24°N in the North Pacific (Fig. 24). This observed spectrum has maximum levels along a non-dispersive line with effective propagation speed that, as anticipated, is equal to or greater than the local theoretical long-wave speed estimates. The corresponding zonal-average observed SSH standard deviation is substantially greater than 0.02 m (Fig. 1), consistent with

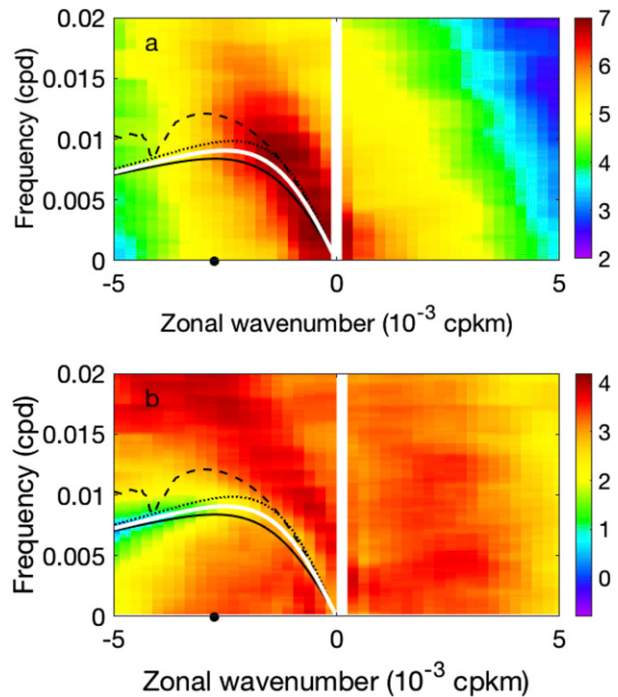


FIG. 24. As in Fig. 2, but along 24°N between 125° and 165°E in the western North Pacific, and with $L_R \approx 58$ km from Chelton et al. (1998), and $c_{R^*} \approx -0.09$ m s $^{-1}$ and $\lambda_*/(2\pi) \approx 63$ km in the empirical linear dispersion relation. (a) After Fig. 4 of Early et al. (2011), with increased wavenumber range.

dynamics that are more nonlinear than those represented by the $\beta = 2.4$, $r_\psi = 0.07$, $\tau = 1$ solution. The corresponding observed inverted power spectrum shows a sharp reduction in power along the linear dispersion relation (Fig. 24), which would also be consistent with a greater degree of nonlinearity than in the $\beta = 2.4$ model solution.

The basic structure of maximum spectral level along a nondispersive line with effective propagation speed equal to or greater than the local theoretical long-wave speed estimates is evident also in the wavenumber–frequency spectrum at 24.5°N in the North Pacific computed by Fu (2004) directly from along-track SSH data from the TOPEX/Poseidon altimeter. At the lower spectral levels away from the maximum, the power isolines for $k > 0$ for this observed spectral estimate are roughly independent of frequency, consistent with the unsmoothed model output (Fig. 17). There are other differences in the data processing and spectral estimate that could also contribute to the different spectral structure, but the similarity between this feature of the Fu (2004) spectral estimate and the model spectral structure would seem to be consistent with the inference that the effect of the space–time smoothing along long-wave characteristics in the data processing procedures

may be visible in the wavenumber–frequency spectra computed from the AVISO data.

9. Discussion

A fundamental challenge to understanding the dynamics of ocean mesoscale variability is that neither the effective forcing rate—the flux of energy into the mesoscale field from other scales or sources—nor the effective damping rate is known. A third element of uncertainty is that the space and time scales of the effective forcing are not known. In the configuration explored here, the effective forcing is constrained for all simulations to a band of wavenumbers near the dimensionless deformation radius wavenumber $K = 1$, a restriction that is motivated partly by the need to simplify the problem and partly by an appeal to baroclinic instability of the mean field near the deformation radius as the likely dominant source of mesoscale energy (e.g., Gill et al. 1974; Smith 2007; Tulloch et al. 2011; Venaille et al. 2011). This leaves the stochastic time scale τ as the single model parameter describing physical variations in the statistics of the spatiotemporal structure of the effective forcing.

The comparisons of the solutions of (7) with amplitude, autocorrelation, eddy, and spectral statistics derived from the AVISO SSH dataset suggest that, away from boundary currents and their extensions, the midlatitude ocean mesoscale regime is characterized by a stochastic SSH forcing rate $\sigma_W \approx 1.8 \times 10^{-5} \text{ m s}^{-1}$, an SSH damping rate $r_{\psi*} \leq 1/62 \text{ week}^{-1}$, and a stochastic forcing autocorrelation time scale $\tau_* \geq L_R/U \approx 1 \text{ week}$. The SSH forcing rate σ_W is perhaps more intuitively accessible when expressed as the equivalent SSH variance accumulation rate, $\sigma_W^2 \approx 3.2 \times 10^{-10} \text{ m}^2 \text{ s}^{-1} \approx 1/4 \text{ cm}^2 \text{ day}^{-1}$. This variance accumulates in the band of forcing wavenumbers, through an effectively stochastic process with autocorrelation time scale τ_* .

The model stochastic forcing thus evidently represents a physical process that supports a continuous production of roughly 1 cm^2 of SSH variance every 4 days at wavelengths near $2\pi L_R \approx 200\text{--}400 \text{ km}$, with the fluctuations containing the generated variance having time scales of a week or longer. These estimates are derived under the approximation that the mesoscale variance is entirely contained in the equivalent gravest-mode or equivalent-barotropic structure represented by the single moving layer in the reduced-gravity model, and could be altered in various ways by exchanges and distributions of energy with other vertical-mode structures that are not represented in the model. The absence of these latter interactions and the associated baroclinic eddy instability mechanisms is one possible source of the discrepancy between the observed and modeled eddy

number distributions versus lifetime, with the model producing relatively more long-lived eddies and relatively fewer short-lived eddies than in the observations.

The spatial scales of the forcing in these simulations were imposed, but the relatively long inferred forcing time scale, equal to or greater than the mesoscale advective time scale, appears independently consistent with the identification of baroclinic instability of the large-scale fields as the primary variance production mechanism. As the forcing time scale increases past the mesoscale advective time scale, broader correlations begin to develop between the forcing and the dynamically evolving field, beyond those between the forcing and the immediate, locally generated, forced response that must always exist to support the stochastic variance production. The variance, or energy, production then begins to depend not only on the stochastic forcing rate but also on the correlation of the forcing and the dynamically evolving field, and the equilibrium amplitude response can no longer be computed accurately from the forcing and damping rates alone, as in (17). The ocean mesoscale regime appears therefore to fall at the edge of, or just outside, the stochastic limit, so that wave-mean interaction is just strong enough to begin to reduce the local mesoscale variance production, but is still weak relative to the overall nonlinearity.

The inferred SSH damping rate of $r_{\psi*} \approx 1/62 \text{ week}^{-1}$ is less than half that estimated by Samelson et al. (2016), a decrease that is consistent with the inverse-square root dependence (17) of amplitude response on damping rate and the 50% decrease in the inferred forcing rate σ_W relative to that estimated by Samelson et al. (2016). The physical processes represented by this simplified linear damping rate are not easily identified. Possible contributing processes include bottom friction (Arbic and Flierl 2004) and gravity or lee wave generation from flow over bottom topography (Trossman et al. 2016). It is intriguing to note that the inferred value is roughly comparable to the estimated eddy damping rates from surface current effects on wind stress (Gaube et al. 2015; Dewar and Flierl 1987). Thus, effective drag at the ocean surface, rather than the sea floor, may be a fundamental element of the mesoscale energy balance, which could be consistent with observational evidence for the weakness of mesoscale velocity variability near the sea floor (e.g., LaCasce 2017; de La Lama et al. 2016; Wunsch 1997) if the surface intensification supports relatively efficient energy extraction but the decay time scale is long enough that the vertical distribution of eddy energy is not strongly affected. Another candidate mechanism is the propagation of energy out of the ocean interior, to regions such as western boundaries where dissipation may be enhanced, a process that is not represented in the

doubly-periodic geometry considered here. For example, the simulations of [Early et al. \(2011\)](#), which were conducted in an effectively open domain with dissipation at the edges, show a westward-increasing energy level similar to that apparent in the observed mid-latitude SSH variance ([Fig. 1](#); see also Fig. 2 of [Chelton and Schlax 1996](#) and Fig. 12 of [Fu and Chelton 2001](#)).

The different apparent effects of the nonlinearity on the energy balance, the propagation characteristics and the autocorrelation structure of the model fields are nearly paradoxical. On the one hand, the reduction of the damping rate relative to the linear model estimate from [Samelson et al. \(2016\)](#) implies that part of the autocorrelation decay in the numerical simulations must arise from the nonlinearity in [\(7\)](#), that is, from the advection of relative vorticity and the associated advective scrambling of the potential vorticity and streamfunction fields. On the other hand, the dominance of nondispersive propagation in the nonlinear simulations suggests that the local time rate of change of the relative vorticity must evidently be negligible in the mean, as it should otherwise lead to wave dispersion. In either case, the nonlinearity has no direct influence on the energy balance, as the spatial integral of $\psi J(\psi, \nabla^2\psi)$ vanishes identically in the doubly-periodic geometry, and the amplitude of the nonlinear solution is essentially set a priori—in the stochastic limit $\tau \ll 1$ —just as it is for the linear model, by the balance between the fixed stochastic variance production rate and the damping rate.

A speculative resolution of this apparent paradox, partly informed by visual examination of the propagating ψ and q fields, is that the relative vorticity behaves differently in the regions inside and outside of the dominant, propagating eddy structures. The eddies are approximately axisymmetric and may be assumed to have approximately constant SSH curvature with respect to the eddy-relative radial coordinate, giving an approximate local proportionality between q and ψ that removes the short-wave dispersion from the linear dynamics, in local analogy to isolated coherent eddy theories (e.g., [Larichev and Reznik 1976](#)). In the regions between the eddies, and during eddy growth and decay events, relative vorticity gradients and the consequent nonlinearity may be large. Such a splitting of the relative vorticity field would appear potentially consistent both with the nondispersive propagation characteristics and with the nonlinear enhancement of the autocorrelation decay.

10. Summary

The primary goal of this study was to reconcile the semiempirical stochastic model results of [Samelson et al. \(2014, 2016\)](#) with a consistent dynamical model of the

ocean mesoscale. The comparisons with eddy statistics show that a correspondence between the numerical simulations from the dynamical model [\(7\)](#) and the observations can be obtained that is broadly similar to the correspondence between the semiempirical stochastic model results and the observations. The dynamical and semiempirical models are both forced stochastically, with the forcing in both taken to represent internal dynamical interactions, while the linear wave propagation included in the semiempirical model is consistent with the long-wave limit of the dynamical model. From this point of view, the reduced-gravity model [\(7\)](#) can be seen as an extension of the semiempirical model that incorporates the basic elements of relative vorticity dynamics and advective nonlinearity while retaining the elements of stochastic forcing and long-wave propagation.

The general correspondence between the eddy statistics from the dynamical and semiempirical models and from the observations is therefore persuasive evidence that the original stochastic amplitude model of [Samelson et al. \(2014\)](#)—the simplest of the three systems—effectively extracts the essential, determining characteristics of the processes supporting the evolution of mesoscale eddy variability both in the ocean and in the dynamical model. Among these characteristics is the remarkable simplicity of the normalized mean eddy amplitude, length scale, and rotational-speed life cycles, with their nearly exact time-reversal symmetry and universality for eddy lifetimes of 16–80 weeks. Evidently, the quasigeostrophic nonlinearity produces, in the mesoscale ocean regime, essentially the same stochastic eddy evolution dynamics that are encoded explicitly in the linear stochastic model as a minimal representation of the observed eddy evolution characteristics.

For the reduced-gravity quasigeostrophic model [\(7\)](#) as configured here, the simulations that nominally best reproduce the global-mean midlatitude statistics derived from the AVISO merged dataset of satellite altimeter SSH measurements have parameters in the range $\beta \approx 0.6$, $r_\psi = 0.02$, $\tau \geq 1$, corresponding at 35° latitude and for $L_R = 40$ km to a dimensional SSH stochastic-forcing variance production rate $1/4 \text{ cm}^2 \text{ day}^{-1}$, an SSH damping rate $1/62 \text{ week}^{-1}$, and a stochastic forcing autocorrelation time scale of 1 week or greater. The nonlinear removal of energy from the resonant linear wave field is directly apparent in the linearly-inverted SSH spectra for these simulations and is also clearly resolved by the AVISO SSH dataset. This ocean mesoscale regime of the reduced-gravity quasigeostrophic model is identified as a specific candidate for further theoretical and numerical study of ocean mesoscale dynamics.

Further study of the details of the wavenumber-frequency spectral characteristics of the altimeter data

is also indicated. The mesoscale regime exists near the nominal 200-km spatial and 30-day temporal resolution limits of the gridded altimeter dataset, where the smoothing and interpolation inherent in development of a gridded dataset from the individual altimeter measurements is likely and, toward smaller scales, eventually certain to affect the observed fields to which the simulations are to be compared. For example, space–time smoothing of the model output prior to analysis was seen to affect the comparisons in ways that were in part similar to increasing the stochastic time scale τ , leading to ambiguities in estimation of the best-fit parameters. Similar ambiguities and effects may arise from the filtering used in the altimeter data processing. Some spectral features apparent in the linear-inverted observed spectra seemed possibly to retain a signature of the propagating space–time filtering from the objective analysis procedure used to produce the merged, gridded, SSH dataset, suggesting the possibility that additional information relevant to the comparisons might be present in the unfiltered altimeter data. If so, it is possible that this information might be extracted by other data-analytical methods and used to further constrain the dynamical model. SSH measurements from future advanced, high-resolution satellite altimeters such as that of the planned Surface Water and Ocean Topography (Durand et al. 2010) mission will likely be of great value in definitively constraining these subtle but important characteristics of mesoscale ocean variability.

More broadly, this study is intended as a step toward a future, more complete understanding of the dynamics of the ocean mesoscale. Of special importance in this broader context are the mechanisms governing mesoscale eddy transport and diffusion processes, which remain poorly understood. The parameterization of their effect on larger-scale fields is known to be an important source of uncertainty in projections of the trajectory of Earth's future climate. Further study of a well-constrained, quasi-equilibrium dynamical model of the ocean mesoscale should yield new qualitative and quantitative insights into these processes and their role in ocean circulation and climate. These future extensions and refinements will need to address the systematic regional variations in ocean mesoscale variability, including the distinct eddy fields associated with eastern and western boundary current systems, which are here subsumed into the single, global midlatitude mean that is taken as the statistical definition of the ocean mesoscale regime.

Acknowledgments. We are grateful to Brian Arbic and an anonymous reviewer for constructive comments that helped to refine the presentation. Support for this

research was provided as part of the National Aeronautics and Space Administration (NASA) Ocean Surface Topography and Surface Water and Ocean Topography Science Team activities through NASA Grants NNX13AD78G and NNX16AH76G.

APPENDIX

Scaling, Smoothing, and Supplemental Spectra

a. Scaling

Let $\mathcal{F} = A\mathcal{F}_0/\tau^{1/2}$ for some constant A , and let \mathcal{D} have the form (5), so that (1) takes the form

$$\begin{aligned} & \frac{\partial}{\partial t'}(\nabla'^2\psi' - F_1\psi') + \beta'\frac{\partial\psi'}{\partial x'} + J'(\psi', \nabla'^2\psi') \\ &= \frac{A}{\tau^{1/2}}\mathcal{F}_0 + r'_\psi\psi' - r'_6\nabla'^6\psi'. \end{aligned} \quad (\text{A1})$$

Equation (A1) transforms to (7) through the rescaling $\psi' = P\psi$, $t' = Tt$, $(x', y') = D(x, y)$, where $P = A^{2/3}F_1^{-1}$, $T = A^{-2/3}$, $D = F_1^{-1/2}$. Note that for $T = D/U_A$, this gives $U_A = A^{-2/3}F_1^{-1/2}$ and $P = U_A D$, so this is a consistent rescaling of the original nondimensionalization. Two cases are of interest.

First, (A1) takes the form used by Morten et al. (2017) if the choice $A = \tau_{M3}^{1/2}$, $F_1 = k_d^2$ is made. The equivalent dimensionless parameters in the unprimed-variable form of (7) may then be computed from those in (A1) by the formulas given in the text.

Second, with $F_1 = 1$ the rescaling is determined by the forcing amplitude alone. The equivalent dimensionless parameters in (7) are then obtained from those in (A1) according to $\beta = A^{-2/3}\beta'$, $\tau = A^{2/3}\tau'$, $(r_\psi, r_6) = A^{-2/3}(r'_\psi, r'_6)$. After the analysis of the $\beta \approx 0.6$ simulations was completed, a minor error in the normalization of \mathcal{F}_0 was found, the effect of which was equivalent to setting $A \approx 0.9$ in (A1), rather than the value $A = 1$ that would yield (7) directly. This rescaling of the $\beta \approx 0.6$ simulations was subsequently used to obtain the equivalent dimensionless parameter and variable values for (7), with a subset of the simulations also repeated with the correct normalization of \mathcal{F}_0 to confirm the rescaling. The equivalent, rescaled values have been used in the text to describe the $\beta \approx 0.6$ simulations by reference to (7).

b. Space–time smoothing

Consider a space–time smoothing function $W_X(x, t)$ in the zonal spatial coordinate x and time t ,

$$W_X(x, t) = \frac{1}{\sqrt{\pi}L} \delta(x - c_0 t) \exp\left[-\left(\frac{x}{L}\right)^2\right], \quad (\text{A2})$$

where $\delta(x)$ is the Dirac- δ distribution over x and c_0 is a constant wave speed, with $c_0 < 0$ for westward propagation. Smoothing in space, with scale L , is then carried out along the characteristic $X(t) = c_0 t$, on which $x - c_0 t = 0$. For this spatial smoothing operation, the distance along the characteristic is computed according to the exponential in (A2) as the spatial distance between points on the characteristic, independent of differences in the time coordinate t ; in effect, the characteristic is projected from the (x, t) plane onto the x axis for the purposes of computing this distance.

The corresponding filter transfer function $\hat{W}_X(k, \omega)$ is the Fourier transform of $W_X(x, t)$,

$$\hat{W}_X(k, \omega) = \iint e^{-ikx+i\omega t} W_X(x, t) dx dt, \quad (\text{A3})$$

where the signs of the transforms are chosen opposite so that $\omega = kc$ gives a Fourier component propagating with speed c ($dx = c dt$). For the function W_X from (A2), the transform (A3) gives

$$\hat{W}_X(k, \omega) = \exp\left[-\frac{1}{4}L^2(k - c_0^{-1}\omega)^2\right]. \quad (\text{A4})$$

The pure time smoothing at fixed x may also be represented as a space-time smoothing function $W_t(x, t)$, where

$$W_t(x, t) = \frac{1}{\sqrt{\pi T}} \delta(x) \exp\left[-\left(\frac{t}{T}\right)^2\right], \quad (\text{A5})$$

with transform

$$\hat{W}_t(k, \omega) = \exp\left(-\frac{1}{4}T^2\omega^2\right), \quad (\text{A6})$$

which has no dependence on k .

The $x-t$ space-time smoothing function used for filtering the simulation output can be written as a single function $W_{Xt}(x, t; x', t')$, where

$$W_{Xt}(x, t; x', t') = \frac{1}{\pi LT} \delta(x - c_0 t) \exp\left[-\left(\frac{x}{L}\right)^2\right] \delta(x') \times \exp\left[-\left(\frac{t'}{T}\right)^2\right], \quad (\text{A7})$$

so that $W_{Xt}(x, t; x', t')$ is essentially the product of the two smoothing functions $W_X(x, t)$ and $W_t(x, t)$, with the second set of space-time variables (x', t') introduced to allow the second smoothing operation. The filter transfer function is then obtained by two sequential space-time Fourier transforms,

$$\begin{aligned} \hat{W}_{Xt}(k, \omega) &= \iint e^{-ikx'+i\omega t'} \iint e^{-ikx+i\omega t} \\ &\quad \times W_{Xt}(x, t; x', t') dx dt dx' dt', \end{aligned} \quad (\text{A8})$$

and can be obtained as the product of (A4) and (A6),

$$\begin{aligned} \hat{W}_{Xt}(k, \omega) &= \hat{W}_X(k, \omega) \hat{W}_t(k, \omega) \\ &= \exp\left[-\frac{1}{4}L^2(k - c_0^{-1}\omega)^2 - \frac{1}{4}T^2\omega^2\right]. \end{aligned} \quad (\text{A9})$$

A meridional smoothing factor $\exp(-y^2/L^2)$ can be included but, as long as the characteristics are purely zonal, is independent of t and results in a transformed factor $\exp[-(1/4)L^2l^2]$, where l is meridional wavenumber.

To allow eddy analysis of the smoothed fields, the filtering of the simulation output fields was conducted in space-time coordinates using the numerical equivalent of the functions (A7) with the additional meridional smoothing, and the spectra of the smoothed fields were then computed. The numerical implementation used a Parzen filter in place of a Gaussian, which the former closely approximates (see, e.g., appendix C of Chelton et al. 2019). The space-time filter used here consists of an initial zonal and meridional smoothing with half-power wavelength 65 km, followed by smoothing along zonal modified-long-wave characteristics with half-power wavelength 200 km, and finally smoothing in time with half-power period 30 days. (Only the 65-km smoothing step was carried out for the spatially smoothed component of the blended solution in Figs. 22c and 22d.) Each smoothing step is carried out using a Parzen smoother. The Gaussian decay scales L_G and T_G that correspond to Parzen-smoother half-power wavelengths and periods L_P and T_P may be computed from Eq. (C.5) of Chelton et al. (2019):

$$(L_G, T_G) = 0.187(L_P, T_P). \quad (\text{A10})$$

Thus, for Parzen-smoother half-power wavelength $L_P = 200$ km and period $T_P = 30$ days, the corresponding Gaussian decay scales are $L_G = 37.4$ km and $T_G = 5.6$ days.

c. Kinetic energy spectra

Morten et al. (2017) exhibit the nondispersive line structure in model spectra of kinetic energy, rather than streamfunction or SSH. The additional factor of squared wavenumber in the kinetic energy spectral density does not affect the spectral comparison, except perhaps to suggest more clearly the extension of

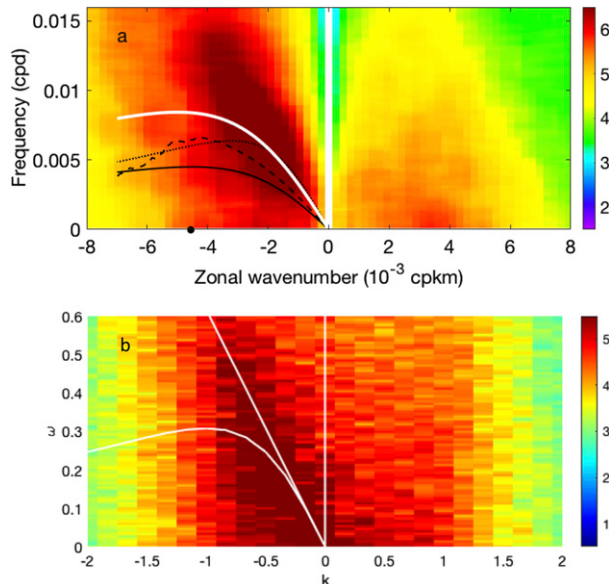


FIG. A1. (a) As in Fig. 2a, but for kinetic energy, computed as $k^2 \times |\dot{\eta}_*|^2$ for zonal wavenumber k (10^{-3} cpkm). (b) As in Fig. 17a, but for dimensionless model kinetic energy, computed as $K^2 \times |\dot{\eta}_*|^2$ for dimensionless wavenumber magnitude K .

the nondispersive spectral line toward small scales (Fig. A1). The comparison of the kinetic energy spectra is complicated slightly by the absence of meridional wavenumber information for the observed zonal-wavenumber spectra, which leads to a presumably artificial minimum in the observed kinetic energy spectral density near zero zonal wavenumber (Fig. A1a).

d. Empirical dispersion relations

For the empirical dispersion relations shown in Figs. 20 and 21, the parameters $c_{R*}, \lambda_*/(2\pi)$; in units of centimeters per second (cm s^{-1}), kilometers (km) are, respectively:

South Pacific 45°S, 150°–110°W: -1.5, 32;
South Indian 40°S, 80°–110°E: -2.1, 40;
South Pacific 38°S, 130°–100°W: -1.8, 45;
South Indian 35°S, 40°–85°E: -3.4, 32;
North Pacific 33°N, 180°–130°W: -2.6, 53;
South Atlantic 33°S, 50°W–0°: -3.6, 40;
North Atlantic 30°N, 70°–40°W: -3.5, 40;
South Pacific 30°S, 170°E–12°W: -3.8, 53;
South Indian 30°S, 60°–100°E: -4.1, 40;
North Pacific 24°N, 125°–165°E: -7.2, 64;
South Pacific 24°S, 160°E–13°W: -6.1, 64;
North Atlantic 24°N, 60°–30°W: -5, 53;
South Atlantic 24°S, 40°W–0°: -5.4, 53;
South Indian 24°S, 50°–100°E: -6.5, 64;
North Pacific 21°N, 130°E–170°W: -7.6, 80;
South Indian 14°S, 70°–120°E: -14.3, 80.

REFERENCES

- Arbic, B. K., and G. R. Flierl, 2004: Baroclinically unstable geostrophic turbulence in the limits of strong and weak bottom Ekman friction: Application to midocean eddies. *J. Phys. Oceanogr.*, **34**, 2257–2273, [https://doi.org/10.1175/1520-0485\(2004\)034<2257:BUGTIT>2.0.CO;2](https://doi.org/10.1175/1520-0485(2004)034<2257:BUGTIT>2.0.CO;2).
- , K. L. Polzin, R. B. Scott, J. G. Richman, and J. F. Shriver, 2013: On eddy viscosity, energy cascades, and the horizontal resolution of gridded satellite altimeter products. *J. Phys. Oceanogr.*, **43**, 283–300, <https://doi.org/10.1175/JPO-D-11-0240.1>.
- Berloff, P., and I. Kamenkovich, 2013: On spectral analysis of mesoscale eddies. Part II: Nonlinear analysis. *J. Phys. Oceanogr.*, **43**, 2528–2544, <https://doi.org/10.1175/JPO-D-12-0233.1>.
- Chelton, D. B., and M. G. Schlax, 1996: Global observations of oceanic Rossby waves. *Science*, **272**, 234–238, <https://doi.org/10.1126/science.272.5259.234>.
- , R. A. de Szoeke, M. G. Schlax, K. E. Naggar, and N. Siwertz, 1998: Geographical variability of the first-baroclinic Rossby radius of deformation. *J. Phys. Oceanogr.*, **28**, 433–460, [https://doi.org/10.1175/1520-0485\(1998\)028<0433:GVOTFB>2.0.CO;2](https://doi.org/10.1175/1520-0485(1998)028<0433:GVOTFB>2.0.CO;2).
- , M. G. Schlax, R. M. Samelson, and R. A. de Szoeke, 2007: Global observations of large oceanic eddies. *Geophys. Res. Lett.*, **34**, L15606, <https://doi.org/10.1029/2007GL030812>.
- , P. Gaube, M. G. Schlax, J. J. Early, and R. M. Samelson, 2011a: The influence of nonlinear mesoscale eddies on near-surface oceanic chlorophyll. *Science*, **334**, 328–332, <https://doi.org/10.1126/science.1208897>.
- , M. G. Schlax, and R. M. Samelson, 2011b: Global observations of nonlinear mesoscale eddies. *Prog. Oceanogr.*, **91**, 167–216, <https://doi.org/10.1016/j.pocean.2011.01.002>.
- , —, —, J. T. Farrar, M. J. Molemaker, J. C. McWilliams, and J. Gula, 2019: Prospects for future satellite estimation of small-scale variability of ocean surface velocity and vorticity. *Prog. Oceanogr.*, **173**, 256–350, <https://doi.org/10.1016/j.pocean.2018.10.012>.
- de La Lama, M. S., J. H. LaCasce, and H. K. Fuhr, 2016: The vertical structure of ocean eddies. *Dyn. Stat. Climate Syst.*, **1**, dzw001, <https://doi.org/10.1093/climsys/dzw001>.
- Dewar, W. K., and G. R. Flierl, 1987: Some effects of the wind on rings. *J. Phys. Oceanogr.*, **17**, 1653–1667, [https://doi.org/10.1175/1520-0485\(1987\)017<1653:SEOTWO>2.0.CO;2](https://doi.org/10.1175/1520-0485(1987)017<1653:SEOTWO>2.0.CO;2).
- Ducet, N., P. Y. Le Traon, and G. Reverdin, 2000: Global high-resolution mapping of ocean circulation from TOPEX/Poseidon and ERS-1 and -2. *J. Geophys. Res.*, **105**, 19 477–19 498, <https://doi.org/10.1029/2000JC900063>.
- Durand, M., L.-L. Fu, D. P. Lettenmaier, D. E. Alsdorf, E. Rodriguez, and D. Esteban-Fernandez, 2010: The Surface Water and Ocean Topography mission: Observing terrestrial surface water and oceanic submesoscale eddies. *Proc. IEEE*, **98**, 766–779, <https://doi.org/10.1109/JPROC.2010.2043031>.
- Early, J. J., R. M. Samelson, and D. B. Chelton, 2011: The evolution and propagation of quasigeostrophic ocean eddies. *J. Phys. Oceanogr.*, **41**, 1535–1555, <https://doi.org/10.1175/2011JPO4601.1>.
- Fu, L.-L., 2004: Latitudinal and frequency characteristics of the westward propagation of large-scale oceanic variability. *J. Phys. Oceanogr.*, **34**, 1907–1921, [https://doi.org/10.1175/1520-0485\(2004\)034<1907:LAFCOT>2.0.CO;2](https://doi.org/10.1175/1520-0485(2004)034<1907:LAFCOT>2.0.CO;2).
- , and D. B. Chelton, 2001: Large-scale ocean circulation. *Satellite Altimetry and Earth Sciences*, L.-L. Fu and A. Cazenave, Eds., International Geophysics, Vol. 69, Academic Press, 133–169.

- Gaube, P., D. B. Chelton, R. M. Samelson, M. G. Schlax, and L. W. O'Neill, 2015: Satellite observations of mesoscale eddy-induced Ekman pumping. *J. Phys. Oceanogr.*, **45**, 104–132, <https://doi.org/10.1175/JPO-D-14-0032.1>.
- Gill, A., J. Green, and A. Simmons, 1974: Energy partition in the large-scale ocean circulation and the production of mid-ocean eddies. *Deep-Sea Res. Oceanogr. Abstr.*, **21**, 499–528, [https://doi.org/10.1016/0011-7471\(74\)90010-2](https://doi.org/10.1016/0011-7471(74)90010-2).
- Killworth, P. D., D. B. Chelton, and R. A. de Szoeke, 1997: The speed of observed and theoretical long extratropical planetary waves. *J. Phys. Oceanogr.*, **27**, 1946–1966, [https://doi.org/10.1175/1520-0485\(1997\)027<1946:TSOOAT>2.0.CO;2](https://doi.org/10.1175/1520-0485(1997)027<1946:TSOOAT>2.0.CO;2).
- LaCasce, J. H., 2017: The prevalence of oceanic surface modes. *Geophys. Res. Lett.*, **44**, 11 097–11 105, <https://doi.org/10.1002/2017GL075430>.
- Larichev, V. D., and G. M. Reznik, 1976: On two-dimensional solitary Rossby waves. *Dokl. Akad. Nauk*, **231** (5), 1077–1079.
- Le Traon, P. Y., Y. Faugère, F. Hernandez, J. Dorandeu, F. Mertz, and M. Ablain, 2003: Can we merge GEOSAT Follow-On with TOPEX/Poseidon and ERS-2 for an improved description of the ocean circulation? *J. Atmos. Oceanic Technol.*, **20**, 889–895, [https://doi.org/10.1175/1520-0426\(2003\)020<0889:CWGMGF>2.0.CO;2](https://doi.org/10.1175/1520-0426(2003)020<0889:CWGMGF>2.0.CO;2).
- Lilly, D. K., 1969: Numerical simulation of two-dimensional turbulence. *Phys. Fluids*, **12**, II-240–II-249, <https://doi.org/10.1063/1.1692444>.
- McWilliams, J. C., and G. R. Flierl, 1979: On the evolution of isolated, nonlinear vortices. *J. Phys. Oceanogr.*, **9**, 1155–1182, [https://doi.org/10.1175/1520-0485\(1979\)009<1155:OTEONI>2.0.CO;2](https://doi.org/10.1175/1520-0485(1979)009<1155:OTEONI>2.0.CO;2).
- , and J. H. S. Chow, 1981: Equilibrium geostrophic turbulence. I: A reference solution in a β -plane channel. *J. Phys. Oceanogr.*, **11**, 921–949, [https://doi.org/10.1175/1520-0485\(1981\)011<0921:EGTIAR>2.0.CO;2](https://doi.org/10.1175/1520-0485(1981)011<0921:EGTIAR>2.0.CO;2).
- Morss, R. E., C. Snyder, and R. Rotunno, 2009: Spectra, spatial scales, and predictability in a quasigeostrophic model. *J. Atmos. Sci.*, **66**, 3115–3130, <https://doi.org/10.1175/2009JAS3057.1>.
- Morten, A. J., B. K. Arbic, and G. R. Flierl, 2017: Wavenumber-frequency analysis of single-layer shallow-water beta-plane quasi-geostrophic turbulence. *Phys. Fluids*, **29**, 106602, <https://doi.org/10.1063/1.5003846>.
- Oh, S., J. Pedlosky, and R. M. Samelson, 1993: Linear and finite-amplitude localized baroclinic instability. *J. Atmos. Sci.*, **50**, 2772–2784, [https://doi.org/10.1175/1520-0469\(1993\)050<2772:LAFALB>2.0.CO;2](https://doi.org/10.1175/1520-0469(1993)050<2772:LAFALB>2.0.CO;2).
- Pedlosky, J., 1987: *Geophysical Fluid Dynamics*. 2nd ed. Springer, 710 pp.
- Pujol, M.-I., Y. Faugère, G. Taburet, S. Dupuy, C. Pelloquin, M. Ablain, and N. Picot, 2016: DUACS DT2014: The new multi-mission altimeter data set reprocessed over 20 years. *Ocean Sci.*, **12**, 1067–1090, <https://doi.org/10.5194/os-12-1067-2016>.
- Rhines, P. B., 1975: Waves and turbulence on a beta-plane. *J. Fluid Mech.*, **69**, 417–443, <https://doi.org/10.1017/S0022112075001504>.
- , 1979: Geostrophic turbulence. *Annu. Rev. Fluid Mech.*, **11**, 401–441, <https://doi.org/10.1146/annurev.fl.11.010179.002153>.
- Samelson, R. M., and J. Pedlosky, 1990: Local baroclinic instability of flow over variable topography. *J. Fluid Mech.*, **221**, 411–436, <https://doi.org/10.1017/S0022112090003615>.
- , M. G. Schlax, and D. B. Chelton, 2014: Randomness, symmetry, and scaling of mesoscale eddy life cycles. *J. Phys. Oceanogr.*, **44**, 1012–1029, <https://doi.org/10.1175/JPO-D-13-0161.1>; Corrigendum, **44**, 2588–2589, <https://doi.org/10.1175/JPO-D-14-0139.1>.
- , —, and —, 2016: A linear stochastic field model of midlatitude mesoscale variability. *J. Phys. Oceanogr.*, **46**, 3103–3120, <https://doi.org/10.1175/JPO-D-16-0060.1>.
- Simmons, A. J., and B. J. Hoskins, 1978: The life cycles of some nonlinear baroclinic waves. *J. Atmos. Sci.*, **35**, 414–432, [https://doi.org/10.1175/1520-0469\(1978\)035<414:TLCOSN>2.0.CO;2](https://doi.org/10.1175/1520-0469(1978)035<414:TLCOSN>2.0.CO;2).
- Smith, K. S., 2007: The geography of linear baroclinic instability in Earth's oceans. *J. Mar. Res.*, **65**, 655–683, <https://doi.org/10.1357/002224007783649484>.
- , and G. K. Vallis, 2001: The scales and equilibration of mid-ocean eddies: Freely evolving flow. *J. Phys. Oceanogr.*, **31**, 554–571, [https://doi.org/10.1175/1520-0485\(2001\)031<0554:TSEAEOM>2.0.CO;2](https://doi.org/10.1175/1520-0485(2001)031<0554:TSEAEOM>2.0.CO;2).
- , and —, 2002: The scales and equilibration of midocean eddies: Forced-dissipative flow. *J. Phys. Oceanogr.*, **32**, 1699–1720, [https://doi.org/10.1175/1520-0485\(2002\)032<1699:TSEAEOM>2.0.CO;2](https://doi.org/10.1175/1520-0485(2002)032<1699:TSEAEOM>2.0.CO;2).
- Tailleux, R., and J. C. McWilliams, 2001: The effect of bottom pressure decoupling on the speed of extratropical, baroclinic Rossby waves. *J. Phys. Oceanogr.*, **31**, 1461–1476, [https://doi.org/10.1175/1520-0485\(2001\)031<1461:TEOBPD>2.0.CO;2](https://doi.org/10.1175/1520-0485(2001)031<1461:TEOBPD>2.0.CO;2).
- The MODE Group, 1978: The Mid-Ocean Dynamics Experiment. *Deep-Sea Res.*, **25**, 859–910, [https://doi.org/10.1016/0146-6291\(78\)90632-X](https://doi.org/10.1016/0146-6291(78)90632-X).
- Trossman, D. S., B. K. Arbic, J. G. Richman, S. T. Garner, S. R. Jayne, and A. J. Wallcraft, 2016: Impact of topographic internal lee wave drag on an eddying global ocean model. *Ocean Modell.*, **97**, 109–128, <https://doi.org/10.1016/j.ocemod.2015.10.013>.
- Tulloch, R., J. Marshall, C. Hill, and K. S. Smith, 2011: Scales, growth rates and spectral fluxes of baroclinic instability in the ocean. *J. Phys. Oceanogr.*, **41**, 1057–1076, <https://doi.org/10.1175/2011JPO4404.1>.
- Venaille, A., G. K. Vallis, and K. S. Smith, 2011: Baroclinic turbulence in the ocean: Analysis with primitive equation and quasigeostrophic simulations. *J. Phys. Oceanogr.*, **41**, 1605–1623, <https://doi.org/10.1175/JPO-D-10-05021.1>.
- Wortham, C., and C. Wunsch, 2014: A multidimensional spectral description of ocean variability. *J. Phys. Oceanogr.*, **44**, 944–966, <https://doi.org/10.1175/JPO-D-13-0113.1>.
- Wunsch, C., 1997: The vertical partition of oceanic horizontal kinetic energy. *J. Phys. Oceanogr.*, **27**, 1770–1794, [https://doi.org/10.1175/1520-0485\(1997\)027<1770:TVPOOH>2.0.CO;2](https://doi.org/10.1175/1520-0485(1997)027<1770:TVPOOH>2.0.CO;2).
- , 2009: The oceanic variability spectrum and transport trends. *Atmos.–Ocean*, **47**, 281–291, <https://doi.org/10.3137/OC310.2009>.
- Zang, X., and C. Wunsch, 1999: The observed dispersion relationship for North Pacific Rossby wave motions. *J. Phys. Oceanogr.*, **29**, 2183–2190, [https://doi.org/10.1175/1520-0485\(1999\)029<2183:TODRFN>2.0.CO;2](https://doi.org/10.1175/1520-0485(1999)029<2183:TODRFN>2.0.CO;2).